ORNL/TM-10196

ornl

OAK RIDGE
NATIONAL
LABORATORY

MARTIN MARIETTA

Development and Evaluation of a Monte Carlo Code System for Analysis of Ionization Chamber Responses

J. O. Johnson
T. A. Gabriel

OPERATED BY
MARTIN MARIETTA ENERGY SYSTEMS, INC.
FOR THE UNITED STATES
DEPARTMENT OF ENERGY

Printed in the United States of America. Available from
National Technical Information Service
U.S. Department of Commerce
5285 Port Royal Road, Springfield, Virginia 22161
NTIS price codes—Printed Copy A06 Microfiche A01

ORNL/TM-10196

Engineering Physics and Mathematics Division

DEVELOPMENT AND EVALUATION OF A MONTE CARLO CODE SYSTEM FOR ANALYSIS OF IONIZATION CHAMBER RESPONSES

J. O. Johnson
T. A. Gabriel

Date Published: July 1987

This Work Sponsored by
Defense Nuclear Agency
Under
Interagency Agreement No. 40-65-65

Prepared by the
OAK RIDGE NATIONAL LABORATORY
Oak Ridge, Tennessee 37831
operated by
MARTIN MARIETTA ENERGY SYSTEMS, INC.
for the
U.S. DEPARTMENT OF ENERGY
under contract DE-AC05-840R21400

TABLE OF CONTENTS

LIST OF TABLES

TABLE PAGE

LIST OF FIGURES

FIGURE PAGE

FIGURE PAGE

ACKNOWLEDGMENTS

The authors wish to express their sincere appreciation for the many interesting discussions and suggestions contributed by Dr. D. T. Ingersoll, Dr. R. A. Lillie, Ms. M. B. Emmett, and Mr. M. W. Waddell. The authors are especially indebted to Dr. S. N. Cramer who suggested this project and served as a technical consultant. Special thanks are extended to Angie Alford for typing and preparing the many drafts of this manuscript.

Appreciation is also expressed to Dr. D. E. Bartine, Dr. D. G. Cacuci, and the Engineering Physics and Mathematics Division of the Oak Ridge National Laboratory for providing partial funding of this work. The author also wishes to thank Lt. Cmdr. G. H. Zeman, 1Lt. M. A. Dooley, and Mr. D. E. Eagleson of the Armed Forces Radiobiology Research Institute and Cmdr. Bob Devine of the Defense Nuclear Agency for their strong interest and support of this project.

DEVELOPMENT AND EVALUATION OF A MONTE CARLO CODE SYSTEM FOR ANALYSIS OF IONIZATION CHAMBER RESPONSES

ABSTRACT

The purpose of this work is the development and testing of a Monte Carlo code system for calculating the response of an ionization chamber to a mixed neutron and photon radiation environment. The resulting code system entitled MICAP - a Monte Carlo Ionization Chamber Analysis Package - determines the neutron, photon, and total responses of the ionization chamber to the mixed field radiation environment. The Monte Carlo method performs accurate simulations of the physical processes involved in detecting radiation using ionization chambers, and eliminates limitations inherent in approximate methods.

The calculational scheme used in MICAP follows individual radiation particles incident on the ionization chamber wall material. The incident neutrons produce photons and heavy charged particles and both primary and secondary photons produce electrons and positrons. As these charged particles enter or are produced in the chamber cavity material, they lose energy and produce ion pairs until their energy is completely dissipated or until they escape the cavity. Ion recombination effects are included along the path of each charged particle rather than applied as an integral correction to the final result. ENDF/B-V partial cross section data have been incorporated in the neutron transport module to account for all processes which may contribute to the output signal. The transport modules utilize continuous angular distribution and secondary energy distribution data when selecting the emergent direction and energy

of a particle. Furthermore, reactions are treated as discrete and allowed to occur with any of the constituent nuclides comprising a mixture. Finally, MICAP incorporates a combinatorial geometry package and input cross section processors to eliminate restrictions in the modeling capability of the code system with respect to geometry, physical processes, nuclear data, and sources.

To evaluate MICAP, comparisons were made with results obtained using other code systems and with experimental results. Separate comparisons with other code systems verified the validity of the neutron, photon, and charged particle transport processes and the nuclear models used to describe the individual neutron reactions, respectively. Comparisons with mono-energetic photon calibration experiments and with mixed neutron and photon radiation experiments verified the applicability of MICAP for analyzing the response of ionization chambers to mixed field radiation environments.

CHAPTER I

INTRODUCTION

In the field of radiation dosimetry, it is often necessary to establish an accurate relationship between a radiation field and an observed response in order to infer physical quantities such as radiation exposure, energy transfer, or absorbed dose. The relationship depends on the characteristics of the radiation, the irradiated material, and the detection device. Ideally, the detector should not perturb the radiation field, and therefore, provide an observable response in a known and reproducible manner. In practice, however, perturbations must be considered in the interpretation of the detector response.

A type of detector commonly used in dosimetry is the gas-filled ionization chamber. The detector is comprised of a container, a gaseous fill material, and a charge collection system. The container and gas materials are normally selected to closely match the material to be irradiated so as to minimize the perturbing effects of the detector. Because of the relatively low density gas region, these detectors are referred to as "cavity ionization chambers," and the methodology used to determine the response of the detectors is referred to as "cavity chamber theory."[1] Using cavity chamber theory to analytically predict the observed response of the detectors requires some approximate representations of the physical processes occurring within the detectors.

The purpose of the present work is to develop and evaluate a Monte Carlo code system for determining the response of a gas-filled

ionization chamber in a mixed neutron and photon radiation environment. In particular, the code system will calculate the neutron, photon, and total responses of the ionization chamber. The Monte Carlo analysis of an ionization chamber performs accurate simulations of the physical processes involved in detecting radiation and eliminates the limitations inherent in existing deterministic methods based on cavity chamber theory.

1.0 BACKGROUND

The cavity ionization chamber is a gas-filled enclosure in which the incident radiation produces ionization. Within the enclosure, there are two or more electrodes which operate under the influence of an externally applied voltage. As the applied voltage increases, the drift velocities of the electrons freed in the ionization processes increase and ion recombination decreases. At saturation voltage, ion recombination is at a minimum, yet the voltage is not so strong as to cause significant secondary ionization (charge amplification through cascading). Therefore the observed signal is proportional to the total energy deposited by charged particles produced via the incident radiation.

Most analytical and experimental techniques currently used in radiation dosimetry are based on cavity chamber theory. The fundamental assumption of cavity chamber theory is that the dimensions of the cavity are small compared with the ranges of the electrons produced in the ionization processes.[2] More precisely, the theory assumes that the size of the cavity is such that:

1. the electron spectrum established in the enclosing material, i.e. in the chamber wall, is not modified by the presence of the gas in the cavity,
2. electrons generated in the cavity from interactions between the gas and the primary or secondary radiation are negligible, and
3. the primary radiation fluence (neutron and/or photon fluence) is spatially uniform in the region from which secondary electrons enter the cavity.

The analytical and experimental techniques for photons (X-rays and gamma-rays) have been extensively developed throughout the history of radiation dosimetry.[3-5] Hence, accurate determinations of the absorbed dose for numerous photon energies and various source-object configurations are routinely accomplished.

The determination of the absorbed dose associated with a neutron field has not been as extensively studied as that from photons. High and intermediate "mono-energetic" neutron source experiments constitute most of the work. Unlike mono-energetic photon sources which emit photons at discrete energies, neutron sources classified as mono-energetic actually emit a spectral distribution peaked at some energy. Therefore, the interpretation of the absorbed dose data requires knowledge of the incident neutron spectrum and consequently, the accuracy in the determination of the absorbed dose may be compromised. Although the uses of neutron sources in biology and medicine have increased significantly, comparisons of the results from the analytical and experimental techniques used in neutron dosimetry continue to show large discrepancies in the reported

absorbed doses.[6] These discrepancies were evidenced at the International Neutron Dosimetry Intercomparison (INDI)[7] and the European Neutron Dosimetry Intercomparison Project (ENDIP),[8] where most of the available ionization chambers (commercial and research) were evaluated. Two factors which contributed to the observed discrepancies at INDI and ENDIP were the inconsistancies in the experimental procedures used to obtain the measured responses, and the systematic differences in the absolute values of the theoretical parameters used to derive the doses from the ionization chamber measurements.

The measurement of neutron dose is often complicated by the presence of a photon background and because most dosimeters are sensitive to both neutrons and photons.[9-10] Since the biological effects of neutrons and photons are different, the two components must be determined in order to obtain the correct response of the biological system to the mixed field radiation. Ionization chambers used in dosimetry work are usually designed and constructed to satisfy the assumptions associated with cavity chamber theory and to minimize the effects of approximations resulting from the theory. For neutrons, the maximum size of a cavity ionization chamber that satisfies the condition of negligible secondary particle production is inconveniently small. Consequently, analyzing the data from these ionization chambers using cavity chamber theory may produce errors in the neutron dosimetry results. Therefore the various organizations involved in neutron dosimetry adopt different approaches toward determining the absorbed dose. These approaches, although all based on variations of cavity chamber theory, have lead to contradictory results and conclusions.

1.1 NEED FOR THE PRESENT WORK

Recently, the Armed Forces Radiobiology Research Institute (AFRRI) expressed the need for Monte Carlo estimations of detector responses in terms of the electrical charge collected when the ionization chambers are placed in mixed neutron and photon radiation environments. Such radiation environments include nuclear battlefield environments, standard reference radiation fields such as that of the Health Physics Research Reactor (HPRR) at ORNL, those at the Army Pulse Radiation Division (APRD) and AFRRI, and the fields compiled in IAEA Report 180, "Compendium of Neutron Spectra in Criticality Accident Dosimetry."[11] The use of the Monte Carlo method is generally regarded as the best way to avoid the shortcomings of the currently employed methods based on cavity chamber theory.

Existing general Monte Carlo code systems are not tailored to perform the ionization chamber calculations for the radiation fields of interest to AFRRI. The term "general" as applied to Monte Carlo indicates there are few, if any, restrictions in the modeling capability of the code system with respect to geometry, physical processes, nuclear data, and radiation sources. However, even a general Monte Carlo code usually involves problem-dependent user-written subroutines which tailor the code for specific applications.

There are several instances in the literature where specific Monte Carlo codes have been written for detector calculations.[12-14] These codes are limited to specific applications such as augmenting existing results from analytical methods, or providing data needed by the analytical methods. A code written for a specific applica-

tion usually requires a major reprogramming effort before it is applicable to another problem. Furthermore, Monte Carlo codes written for specific applications usually have the nuclear data (cross sections and stopping powers) included in the program itself. This further complicates the effort associated with using the program for a different problem. The advantage of developing a general Monte Carlo code system is the adaptability to a wide range of problems through the use of problem-dependent subroutines. Also, general Monte Carlo code systems would employ data pre-processors to obtain the nuclear data needed for a particular application.

1.2 PROJECT OBJECTIVES

In summary, the objectives of the present work were divided into the following tasks:

1. Develop input data processors for a neutral particle Monte Carlo code to arrange the pointwise data from the Evaluated Nuclear Data File (ENDF) library into a format compatible with the code.
2. Modify an existing neutral particle Monte Carlo code to calculate the physical processes occurring in a typical ionization chamber used in mixed field dosimetry.
3. Develop a Monte Carlo code to calculate charged particle and recoil heavy ion energy loss processes in the ionization chamber.
4. Modify an existing photon-electron Monte Carlo code to calculate the physical processes occurring in the ionization chamber.

5. Use the new code system to generate results that can be compared with experimental data and with results from analytical methods based on cavity chamber theory.

The PXMORSE[15–16] Monte Carlo code (a continuous energy version of MORSE)[17] was chosen as the code to modify for the neutral particle transport calculation, and the EGS[18–19] photon-electron transport module of the high-energy calorimeter Monte Carlo code system was chosen as the code to modify for the photon transport calculation.

1.3 CALCULATIONAL PROCEDURE

The calculational scenario follows the individual radiation particles incident on the ionization chamber wall material. The incident neutrons produce photons and charged particles (protons, alpha particles, recoil ions, etc.), and both the primary and secondary photons produce electrons. As these charged particles and electrons enter or are produced in the chamber cavity material (usually a gas, but possibly a tissue-like substance), they produce ion pairs until their energy is completely dissipated or until they escape the cavity. The number of ion pairs produced is computed using work functions, which are defined as the average energy required to produce an ion pair.[20] The work functions account for charged particle and electron energy loss mechanisms in the detector cavity in addition to ion production. The Monte Carlo model accounts for energy losses from the cavity in the form of delta rays (secondary low-energy electrons), bremsstrahlung photons, or other charged particles producing no ionization. An analytical model by

Birks[21] is incorporated to model any ion recombination effects which might occur. The Birks simulation is performed along each charged particle and/or electron path rather than applied as an integral correction to the final result.

This calculational procedure models the physical processes occurring in gas ionization more accurately than the current analysis methods based on cavity chamber theory. All nuclear data such as cross sections, stopping powers, etc., are utilized in a pointwise manner, which enhances the accuracy of the procedure. Continuous angular distribution and secondary energy distribution data are incorporated for selecting the emergent direction and energy of a particle. Furthermore, reactions are treated as discrete and allowed to occur with any of the constituent nuclides comprising a mixture. Finally, a combinatorial geometry package and input cross section processors are utilized to eliminate restrictions in the modeling capability of the code system with respect to geometry, physical processes, nuclear data, and sources.

1.4 ORIGINALITY OF PRESENT WORK

The final product of the present research is a new code system which provides a unique capability in the area of mixed field dosimetry. The present work incorporates the models of all physical processes occurring in gas ionization into the Monte Carlo random walk procedure. In particular, new and significant capabilities in ionization chamber response calculations are realized by incorporating models describing:

1. ion pair production and charge collection processes,
2. charged particle energy loss mechanisms,
3. charged particle transport and ion recombination effects, and
4. nonelastic-nucleus collisions, i.e. (n,p), (n,d), (n,t), (n,α), etc.

Utilizing all nuclear data such as cross sections, stopping powers, etc. in a pointwise manner yields a more rigorous treatment of the particle transport processes than that available from current methods. By developing a "general" Monte Carlo code system tailored to ionization chamber calculations, the present work will be useful for many applications in the field of radiation dosimetry.

There is presently no computational code system, Monte Carlo or otherwise, that is capable of performing the analysis of radiation dosimetry experiments to the extent developed in the present work. The "specific" Monte Carlo codes usually apply to only one experimental set-up, limit the number of interactions allowed to occur in the analysis, and restrict the experiment to simple geometries, e.g. slab, concentric spheres, or concentric cylinders. The existing general purpose Monte Carlo code systems, i.e. MORSE,[17] MCNP,[22] and TRIPOLI,[23] have all been written for neutral particle transport analysis. As such, these codes concentrate on the interactions affecting the neutron and/or photon flux without regard to the other products (protons, deuterons, alpha particles, etc.) of the interactions. Consequently, these codes do not model the production and transport of the low energy charged particles essential to ionization chamber response analysis. The present work provides a new

computational tool which eliminates most of the shortcomings of the methods currently being used in ionization chamber response analysis.

CHAPTER II

APPLICATION OF MONTE CARLO TO THE SOLUTION OF THE TRANSPORT EQUATION

2.0 BOLTZMANN TRANSPORT EQUATION

The generalized time-dependent integro-differential form of the Boltzmann transport equation can be derived by conserving particles within a differential volume in phase space. More specifically, the derivation equates the net storage of particles within a differential element of phase space ($d\bar{r}dEd\bar{\Omega}$) to the particle gains minus the particle losses. The derivation has been presented in many texts and publications and will briefly be discussed here. The following discussion is based on work presented in S. N. Cramer's dissertation[24] and in D. E. Bartine's dissertation.[25]

The general time-dependent integro-differential form of the Boltzmann transport equation is:

$$\frac{1}{v}\frac{\partial}{\partial t}\phi(\bar{r},E,\bar{\Omega},t) + \bar{\Omega}\cdot\bar{\nabla}\phi(\bar{r},E,\bar{\Omega},t) + \Sigma_t(\bar{r},E)\phi(\bar{r},E,\bar{\Omega},t)$$
$$= Q(\bar{r},E,\bar{\Omega},t) + \iint dE'd\bar{\Omega}'\Sigma_s(\bar{r},E'\rightarrow E,\bar{\Omega}'\rightarrow\bar{\Omega})\phi(\bar{r},E',\bar{\Omega}',t) \quad , \tag{2-1}$$

where $(\bar{r},E,\bar{\Omega},t)$ denotes the general seven-dimensional phase space,

$\bar{r}$ = position variable,

E = the particle's kinetic energy,

v = the particle's speed corresponding to its kinetic energy E,

$\bar{\Omega}$ = a unit vector which describes the particle's direction of motion,

t = time variable,

$\phi(\bar{r},E,\bar{\Omega},t)$ = the time-dependent angular flux,

$\frac{1}{v}\frac{\partial}{\partial t}\phi(\bar{r},E,\bar{\Omega},t)dEd\bar{\Omega}$ = net storage (gains minus losses) per unit volume and time at the space point $\bar{r}$ and time t of particles with energies in dE about E and with directions which lie in $d\bar{\Omega}$ about $\bar{\Omega}$,

$\bar{\Omega}\cdot\bar{\nabla}\phi(\bar{r},E,\bar{\Omega},t)dEd\bar{\Omega}$ = net convection loss per unit volume and time at the space point $\bar{r}$ and time t of particles with energies in dE about E and directions which lie in $d\bar{\Omega}$ about $\bar{\Omega}$,

$\Sigma_t(\bar{r},E)$ = the total cross section at the space point $\bar{r}$ for particles of energy E,

$\Sigma_t(\bar{r},E)\phi(\bar{r},E,\bar{\Omega},t)dEd\bar{\Omega}$ = collision loss per unit volume and time at the space point $\bar{r}$ and time t of particles with energies in dE about E and directions which lie in $d\bar{\Omega}$ about $\bar{\Omega}$,

$\Sigma_s(\bar{r},E'\rightarrow E,\bar{\Omega}'\rightarrow\bar{\Omega})dEd\bar{\Omega}$ = the differential scattering cross section which describes the probability per unit path that a particle with an initial energy E' and an initial direction $\bar{\Omega}'$ undergoes a scattering collision at $\bar{r}$ which places it into a direction that lies in $d\bar{\Omega}$ about $\bar{\Omega}$ with a new energy in dE about E,

$\left[\int\int\Sigma_s(\bar{r},E'\rightarrow E,\bar{\Omega}'\rightarrow\bar{\Omega})\phi(\bar{r},E',\bar{\Omega}',t)dE'd\bar{\Omega}'\right]dEd\bar{\Omega}$ = inscattering gain

per unit volume and time at the space point $\bar{r}$ and time t of particles with energies in dE about E and directions which lie in $d\bar{\Omega}$ about $\bar{\Omega}$, and,

$Q(\bar{r},E,\bar{\Omega},t)dEd\bar{\Omega}$ = source particles emitted per unit volume and time at the space point $\bar{r}$ and time t with energies in dE about E and directions which lie in $d\bar{\Omega}$ about $\bar{\Omega}$.

While Monte Carlo codes are capable of solving the time dependent Boltzmann transport equation, the present work is directed specifically at the solution of the static (time-independent) Boltzmann equation:

$$\bar{\Omega}\cdot\bar{\nabla}\phi(\bar{r},E,\bar{\Omega}) + \Sigma_t(\bar{r},E)\phi(\bar{r},E,\bar{\Omega}) = Q(\bar{r},E,\bar{\Omega}) + \iint dE'\,d\bar{\Omega}'\,\Sigma_s(\bar{r},E'\rightarrow E,\bar{\Omega}'\rightarrow\bar{\Omega})\phi(\bar{r},E',\bar{\Omega}') \quad . \tag{2-2}$$

Equation 2-2 represents the most general form of the static integro-differential Boltzmann transport equation. As such, this equation is directly applicable to neutron transport and for most applications involving photon transport. However, in ionization chamber response analyses, Eq. 2-2 must be modified for photon transport to account for electron production of bremsstrahlung photons and photons produced via neutron interactions. More specifically, the inscatter term in Eq. 2-2 becomes:

$$\iint dE'\,d\bar{\Omega}'\,\Sigma_s(\bar{r},E'\rightarrow E,\bar{\Omega}'\rightarrow\bar{\Omega})\phi(\bar{r},E',\bar{\Omega}') =$$
$$\iint dE'\,d\bar{\Omega}'\,\Sigma_{\gamma\rightarrow\gamma}(\bar{r},E'\rightarrow E,\bar{\Omega}'\rightarrow\bar{\Omega})\phi_\gamma(\bar{r},E',\bar{\Omega}') +$$
$$\iint dE'\,d\bar{\Omega}'\,\Sigma_{e\rightarrow\gamma}(\bar{r},E'\rightarrow E,\bar{\Omega}'\rightarrow\bar{\Omega})\phi_e(\bar{r},E',\bar{\Omega}') +$$

$$\iint dE'\, d\bar{\Omega}'\, \Sigma_{n\to\gamma}(\bar{r},E'\to E,\bar{\Omega}'\to\bar{\Omega})\phi_n(\bar{r},E',\bar{\Omega}') \quad , \tag{2-3}$$

where

$\left[\iint dE'\, d\bar{\Omega}'\, \Sigma_{\gamma\to\gamma}(\bar{r},E'\to E,\bar{\Omega}'\to\bar{\Omega})\phi_\gamma(\bar{r},E',\bar{\Omega}')\right] dE d\bar{\Omega}$ = inscattering gain per unit volume at the space point $\bar{r}$ of photons with energies in dE about E and directions which lie in $d\bar{\Omega}$ about $\bar{\Omega}$,

$\left[\iint dE'\, d\bar{\Omega}'\, \Sigma_{e\to\gamma}(\bar{r},E'\to E,\bar{\Omega}'\to\bar{\Omega})\phi_e(\bar{r},E',\bar{\Omega}')\right] dE d\bar{\Omega}$ = bremsstrahlung scattering gain per unit volume at the space point $\bar{r}$ of photons with energies in dE about E and directions which lie in $d\bar{\Omega}$ about $\bar{\Omega}$,

$\left[\iint dE'\, d\bar{\Omega}'\, \Sigma_{n\to\gamma}(\bar{r},E'\to E,\bar{\Omega}'\to\bar{\Omega})\phi_n(\bar{r},E',\bar{\Omega}')\right] dE d\bar{\Omega}$ = photon production gain per unit volume at the space point $\bar{r}$ of photons with energies in dE about E and directions which lie in $d\bar{\Omega}$ about $\bar{\Omega}$, and

$\phi_\gamma(\bar{r},E,\bar{\Omega})$ = the photon angular flux,

$\phi_e(\bar{r},E,\bar{\Omega})$ = the electron angular flux, and,

$\phi_n(\bar{r},E,\bar{\Omega})$ = the neutron angular flux.

Incorporating Eq. 2-3 into Eq. 2-2 and substituting ϕ_γ for ϕ and Q_γ for Q yields:

$$\begin{aligned}\bar{\Omega}\cdot\bar{\nabla}\phi_\gamma(\bar{r},E,\bar{\Omega}) + \Sigma_t(\bar{r},E)\phi_\gamma(\bar{r},E,\bar{\Omega}) = Q_\gamma(\bar{r},E,\bar{\Omega}) + \\ \iint dE'\, d\bar{\Omega}'\, \Sigma_{\gamma\to\gamma}(\bar{r},E'\to E,\bar{\Omega}'\to\bar{\Omega})\phi_\gamma(\bar{r},E',\bar{\Omega}') + \\ \iint dE'\, d\bar{\Omega}'\, \Sigma_{e\to\gamma}(\bar{r},E'\to E,\bar{\Omega}'\to\bar{\Omega})\phi_e(\bar{r},E',\bar{\Omega}') + \\ \iint dE'\, d\bar{\Omega}'\, \Sigma_{n\to\gamma}(\bar{r},E'\to E,\bar{\Omega}'\to\bar{\Omega})\phi_n(\bar{r},E',\bar{\Omega}') \quad .\end{aligned} \tag{2-4}$$

Equation 2-4 represents the generalized static integro-differential Boltzmann transport equation for photons with bremsstrahlung production.

As in the case with photons, Eq. 2-2 must also be modified for electron transport to account for photon production of electrons via the photoelectric absorption and pair production interactions. Furthermore, at low electron energies, it becomes impractical to simulate discrete electron interactions, and Eq. 2-2 must be modified to include a continuous energy loss term. This difficulty with electron transport arises because the cross sections for most electron interactions become very large as the electron energy approaches zero. The exact values are not well known and it is therefore not feasible to try to simulate every interaction. To properly account for the above considerations, the inscatter term in Eq. 2-2 becomes:

$$\begin{aligned} &\iint dE'\,d\bar{\Omega}'\,\Sigma_s(\bar{r},E'\to E,\bar{\Omega}'\to\bar{\Omega})\,\phi(\bar{r},E',\bar{\Omega}') = \\ &\iint dE'\,d\bar{\Omega}'\,\Sigma_{e\to e}(\bar{r},E'\to E,\bar{\Omega}'\to\bar{\Omega})\,\phi_e(\bar{r},E',\bar{\Omega}') + \\ &\iint dE'\,d\bar{\Omega}'\,\Sigma_{\gamma\to e}(\bar{r},E'\to E,\bar{\Omega}'\to\bar{\Omega})\,\phi_\gamma(\bar{r},E',\bar{\Omega}') + \\ &\frac{\partial}{\partial E}\left[S(E)\,\phi_e(\bar{r},E,\bar{\Omega})\right] , \end{aligned} \tag{2-5}$$

where

$\left[\iint dE'\,d\bar{\Omega}'\,\Sigma_{e\to e}(\bar{r},E'\to E,\bar{\Omega}'\to\bar{\Omega})\,\phi_e(\bar{r},E',\bar{\Omega}')\right] dE\,d\bar{\Omega}$ = inscattering gain per unit volume at the space point $\bar{r}$ of electrons with energies in dE about E and directions which lie in $d\bar{\Omega}$ about $\bar{\Omega}$,

$\left[\iint dE'\,d\bar{\Omega}'\,\Sigma_{\gamma\to e}(\bar{r},E'\to E,\bar{\Omega}'\to\bar{\Omega})\,\phi_\gamma(\bar{r},E',\bar{\Omega}')\right] dE\,d\bar{\Omega}$ = photoelectric absorption and pair production gains per unit volume at the

space point $\bar{\bar{r}}$ of electrons with energies in dE about E and directions which lie in $d\bar{\bar{\Omega}}$ about $\bar{\Omega}$,

$\left[\frac{\partial}{\partial E}\left(S(E)\phi_e(\bar{\bar{r}},E,\bar{\Omega})\right)\right]dEd\bar{\bar{\Omega}}$ = a continuous slowing down per unit volume at the space point $\bar{\bar{r}}$ of electrons with energies in dE about E and directions which lie in $d\bar{\bar{\Omega}}$ about $\bar{\Omega}$,

S(E) = the energy loss per unit pathlength i.e., the stopping power,

$\phi_e(\bar{\bar{r}},E,\bar{\Omega})$ = the electron angular flux, and,

$\phi_\gamma(\bar{\bar{r}},E,\bar{\bar{\Omega}})$ = the photon angular flux.

Incorporating Eq. 2-5 into Eq. 2-2 and substituting ϕ_e for ϕ and Q_e for Q yields:

$$\begin{aligned}\bar{\bar{\Omega}}\cdot\bar{\bar{\nabla}}\phi_e(\bar{\bar{r}},E,\bar{\Omega}) + \Sigma_t(\bar{\bar{r}},E)\phi_e(\bar{\bar{r}},E,\bar{\Omega}) &= Q_e(\bar{\bar{r}},E,\bar{\bar{\Omega}}) + \\ \iint dE'd\bar{\bar{\Omega}}'\Sigma_{e\to e}(\bar{\bar{r}},E'\to E,\bar{\Omega}'\to\bar{\Omega})\phi_e(\bar{\bar{r}},E',\bar{\bar{\Omega}}') &+ \\ \iint dE'd\bar{\bar{\Omega}}'\Sigma_{\gamma\to e}(\bar{\bar{r}},E'\to E,\bar{\Omega}'\to\bar{\Omega})\phi_\gamma(\bar{\bar{r}},E',\bar{\bar{\Omega}}') &+ \\ \frac{\partial}{\partial E}\left[S(E)\phi_e(\bar{\bar{r}},E,\bar{\Omega})\right] .\end{aligned} \tag{2-6}$$

Equation 2-6 represents the generalized static integro-differential Boltzmann transport equation for electrons with continuous slowing down and photoelectric absorption and pair production.

While Eq. 2-6 is written specifically for electron transport, it could apply to any charged particle transport. The difficulty in applying Eq. 2-6 to other charged particles, i.e., protons, alpha particles, recoil heavy ions, etc., is the lack of cross section data. The development of theoretical and empirical formulae to

simulate charged particle transport is not as extensive as that for electron transport. There are, however, numerous theoretical formulae developed for calculating charged particle stopping powers which are used in the present work to simulate charged particle energy deposition processes. Using stopping powers to simulate the charged particle energy deposition processes is acceptable because below 20 MeV the probability for charged particle nuclear interaction is small due to the short tracklengths of the charged particles. These short tracklengths result from the limited range of the charged particles. Consequently, the majority of charged particles would deposit their energy before undergoing a collision. Therefore, for charged particle transport, Eq. 2-6 with ϕ_c substituted for ϕ_e and Q_c substituted for Q_e, can be reduced to:

$$\bar{\Omega}\cdot\bar{\nabla}\phi_c(\bar{r},E,\bar{\Omega}) = Q_c(\bar{r},E,\bar{\Omega}) + \frac{\partial}{\partial E}\left[S(E)\phi_c(\bar{r},E,\bar{\Omega})\right] , \tag{2-7}$$

where

$\phi_c(\bar{r},E,\bar{\Omega})$ = the charged particle angular flux, and,

the definitions of the terms in Eq. 2-6 now apply for charged particles.

In the Monte Carlo method, a transport cross section is used to determine the next collision site. Therefore, a small fictitious transport cross section is incorporated to force the transport of the charged particle to a material boundary. The stopping powers are then used to determine the amount of energy deposited in that material. This yields a charged particle transport equation given by:

$$\bar{\Omega}\cdot\bar{\nabla}\phi_c(\bar{r},E,\bar{\Omega}) + \Sigma_t^*(\bar{r},E)\phi_c(\bar{r},E,\bar{\Omega}) = Q_c(\bar{r},E,\bar{\Omega}) + \iint dE'\,d\bar{\Omega}'\Sigma_t^*(\bar{r},E')\delta(E'\rightarrow E,\bar{\Omega}'\rightarrow\bar{\Omega})\phi_c(\bar{r},E',\bar{\Omega}') + \frac{\partial}{\partial E}\left[S(E)\phi_c(\bar{r},E,\bar{\Omega})\right] , \tag{2-8}$$

where

$\Sigma_t^*(\bar{r},E)\phi(\bar{r},E,\bar{\Omega})dEd\bar{\Omega}$ = fictitious collision loss per unit volume at the space point $\bar{r}$ of charged particles with energies in dE about E and directions which lie in $d\bar{\Omega}$ about $\bar{\Omega}$, and,

$\left[\iint dE'\,d\bar{\Omega}'\Sigma_t^*(\bar{r},E')\delta(E'\rightarrow E,\bar{\Omega}'\rightarrow\bar{\Omega})\phi_c(\bar{r},E',\bar{\Omega}')\right]dEd\bar{\Omega}$ = fictitious inscattering gain per unit volume at the space point $\bar{r}$ of charged particles with energies in dE about E and directions which lie in $d\bar{\Omega}$ abour $\bar{\Omega}$.

Equations 2-2, 2-4, and 2-6 represent the generalized static integro-differential Boltzmann transport equation for neutrons, photons, and electrons respectively. As such, these equations are cross-coupled because of photon production of electrons, and neutron and electron production of photons. Applying the Monte Carlo method to these equations effectively decouples the equations by treating these production terms as part of the source term. In other words, Eq. 2-4 can be reduced to Eq. 2-2 if the source term is defined as:

$$Q(\bar{r},E,\bar{\Omega}) = Q_\gamma^*(\bar{r},E,\bar{\Omega}) + \iint dE'\,d\bar{\Omega}'\Sigma_{e\rightarrow\gamma}(\bar{r},E'\rightarrow E,\bar{\Omega}'\rightarrow\bar{\Omega})\phi_e(\bar{r},E',\bar{\Omega}') + \iint dE'\,d\bar{\Omega}'\Sigma_{n\rightarrow\gamma}(\bar{r},E'\rightarrow E,\bar{\Omega}'\rightarrow\bar{\Omega})\phi_n(\bar{r},E',\bar{\Omega}') , \tag{2-9}$$

where $Q_\gamma^*(\bar{r},E,\bar{\Omega})$ represents the external source of photons. Likewise, Eq. 2-6 can be reduced to Eq. 2-2 (with the added continuous energy loss term) if the source term is defined as:

$$Q(\bar{r},E,\bar{\Omega}) = Q_e^*(\bar{r},E,\bar{\Omega}) +$$

$$\iint dE'\,d\bar{\Omega}'\,\Sigma_{\gamma-e}(\bar{r},E'\rightarrow E,\bar{\Omega}'\rightarrow\bar{\Omega})\phi_\gamma(\bar{r},E',\bar{\Omega}') \quad , \tag{2-10}$$

where again $Q_e^*(\bar{r},E,\bar{\Omega})$ represents the external source of electrons. In light of the above discussion and because Eq. 2-8 is a simplification of Eq. 2-6, the formal basis for the Monte Carlo transport of all particles is provided by an integral form of Eq. 2-2 with the added continuous energy loss term.

2.1 RANDOM WALK PROCEDURE

The previous section discussed the transport of all particles, i.e., neutrons, photons, electrons, etc., which contribute to the ionization chamber response in a mixed field radiation environment utilizing the integro-differential Boltzmann transport equation. The Monte Carlo method, however, uses an integral form of the Boltzmann transport equation as the formal basis for the random walk procedure. A random walk by a radiation particle is comprised of its birth event, followed by movements from one collision site to the next, and finally terminated by either absorption or leakage from the system. A reasonable basis for the Monte Carlo random walk procedure is the integral emergent particle density equation given by[24]:

$$\chi(\bar{r},E,\bar{\Omega}) = Q(\bar{r},E,\bar{\Omega}) +$$

$$\iint dE'\,d\bar{\Omega}'\,\frac{\Sigma_s(\bar{r},E'\rightarrow E,\bar{\Omega}'\rightarrow\bar{\Omega})}{\Sigma_t(\bar{r},E')}\int_0^\infty dR\,\Sigma_t(\bar{r},E')e^{-\beta(\bar{r},R,E',\bar{\Omega}')}\chi(\bar{r}',E',\bar{\Omega}') \quad , \tag{2-11}$$

where

$\left[\beta(\bar{r},R,E,\bar{\Omega}) \equiv \int_0^R \Sigma_t(\bar{r}-R'\bar{\Omega},E)dR'\right]$ is referred to as the "optical thickness" and represents the number of mean free paths between spatial points $\bar{r}$ and $\bar{r}'$,

$\chi(\bar{r},E,\bar{\Omega})$ is defined as the density of particles leaving a source or emerging from a real collision with phase space coordinates $(\bar{r},E,\bar{\Omega})$,

[R] is a spatial variable which relates a fixed point in space $(\bar{r})$ to an arbitrary point $(\bar{r}')$, and

the definitions of the other terms are given in the discussion of Eq. 2-2 in the previous section.

The fundamental relationship between the emergent particle density in Eq. 2-11 and the flux density is given by:

$$\chi(\bar{r},E,\bar{\Omega}) = Q(\bar{r},E,\bar{\Omega}) + \iint dE'd\bar{\Omega}'\Sigma_s(\bar{r},E'\rightarrow E,\bar{\Omega}'\rightarrow\bar{\Omega})\phi(\bar{r},E',\bar{\Omega}') \quad , \tag{2-12}$$

and the flux density in terms of the emergent particle density is given by:

$$\phi(\bar{r},E,\bar{\Omega}) = \int_0^\infty dR e^{-\beta(\bar{r},R,E,\bar{\Omega})}\chi(\bar{r},E,\bar{\Omega}) \quad . \tag{2-13}$$

A full discussion of the transformation of Eq. 2.2 to Eq. 2-11 is presented in Ref. 24 and will not be repeated here.

The integral emergent particle density equation can be presented in a simpler notation by defining the transport integral operator as:

$$T(\bar{r}',R,E,\bar{\Omega}) \equiv \int_0^\infty dR\Sigma_t(\bar{r},E)e^{-\beta(\bar{r},R,E,\bar{\Omega})}, \tag{2-14}$$

and the collision integral operator as:

$$C(\bar{r},E'\to E,\bar{\Omega}'\to\bar{\Omega}) \equiv \iint dE'd\bar{\Omega}' \frac{\Sigma_s(\bar{r},E'\to E,\bar{\Omega}'\to\bar{\Omega})}{\Sigma_t(\bar{r},E')}. \tag{2-15}$$

The collision integral operator can be rewritten as:

$$C(\bar{r},E'\to E,\bar{\Omega}'\to\bar{\Omega}) \equiv \iint dE'd\bar{\Omega}' \left[\frac{\Sigma_s(\bar{r},E'\to E,\bar{\Omega}'\to\bar{\Omega})}{\Sigma_s(\bar{r},E')}\right]\left[\frac{\Sigma_s(\bar{r},E')}{\Sigma_t(\bar{r},E')}\right], \tag{2-16}$$

where

$$\Sigma_s(\bar{r},E') = \iint dEd\bar{\Omega}\Sigma_s(\bar{r},E'\to E,\bar{\Omega}'\to\bar{\Omega}) . \tag{2-17}$$

In Eq. 2-16, $[\Sigma_s(\bar{r},E'\to E,\bar{\Omega}'\to\bar{\Omega})/\Sigma_s(\bar{r},E')]$ is a normalized joint probability density function used in selecting an emergent particle's new direction and energy and $[\Sigma_s(\bar{r},E')/\Sigma_t(\bar{r},E')]$ is the nonabsorption probability. Introducing the transport and collision operators into Eq. 2-11, the integral emergent particle density equation in operator notation is obtained:

$$\chi(\bar{r},E,\bar{\Omega}) = Q(\bar{r},E,\bar{\Omega}) +$$

$$C(\bar{\bar{r}},E'\rightarrow E,\bar{\Omega}'\rightarrow\bar{\Omega})T(\bar{r}'\rightarrow\bar{r},E',\bar{\Omega}')\chi(\bar{r}',E',\bar{\Omega}') \quad . \tag{2-18}$$

The principal reason for selecting the integral emergent particle density equation for the Monte Carlo random walk is because the source particles are introduced according to the natural distribution.

The implementation of the random walk procedure is accomplished by representing the emergent particle density $\chi(\bar{r},E,\bar{\Omega})$ as a Neuman series:

$$\chi(\bar{\bar{r}},E,\bar{\Omega}) = \sum_{n=0}^{\infty} \chi^{n}(\bar{r},E,\bar{\Omega}) \quad , \tag{2-19}$$

where

$\chi^{n}(\bar{r},E,\bar{\Omega})dEd\bar{\Omega}$ = the density of particles emerging from the nth collision at the space point $\bar{r}$ with energies in dE about E and with directions which lie in $d\bar{\Omega}$ about $\bar{\Omega}$,

$\chi^{0}(\bar{r},E,\bar{\Omega})$ = the natural source distribution $Q(\bar{r},E,\bar{\Omega})$, and,

$\chi^{n}(\bar{r},E,\bar{\Omega}) = C(\bar{\bar{r}},E'\rightarrow E,\bar{\Omega}'\rightarrow\bar{\Omega})T(\bar{\bar{r}}'\rightarrow r,E',\bar{\Omega}')\chi^{n-1}(\bar{r}',E',\bar{\Omega}')$.

The Neuman series solution of Eq. 2-18 implies the following sequence of events:

1. The random walk begins with the selection of the particle's phase space coordinates, involving position $(\bar{r}_0)$, energy (E_0), and direction $(\bar{\Omega}_0)$, according to the joint probability density function associated with the natural source distribution $Q(\bar{r},E,\bar{\Omega})$.

2. A flight distance R is picked from the probability distribution function (pdF) $\left[\Sigma_t(\bar{r},E_0)e^{-\beta(\bar{r},R,E_0,\bar{\Omega}_0)}\right]$ to determine the first collision site $\bar{r}_1$.

3. At the collision site $\bar{r}_1$, a nuclide from N kinds of nuclides in the mixture is selected. The selection of a scattering angle and energy for a particular nuclide will preserve the unique physics of each interaction.

4. Once the nuclide has been selected, the choice is made between an absorption or a scattering reaction according to the nonabsorption probability $\Sigma_s(\bar{r}_1,E_0)/\Sigma_t(\bar{r}_1,E_0)$.

5. If an absorption occurs, the sequence is initiated again for a new particle. If a scattering reaction occurs, a new direction $(\bar{\Omega}_1)$ is selected according to the marginal probability distribution function $\int dE\Sigma_s(\bar{r}_1,E_0\rightarrow E,\bar{\Omega}_0\rightarrow\bar{\Omega})/\Sigma_s(\bar{r}_1,E_0)$. For elastic scattering and inelastic scattering to a discrete level, a new energy (E_1) is determined from the kinematic equations. For all continuum reactions, a new energy (E_1) is determined from the conditional probability distribution function $\Sigma_s(\bar{r}_1,E_0\rightarrow E,\bar{\Omega}_0\rightarrow\bar{\Omega}_1)/\Sigma_s(\bar{r}_1,E_0)$.

6. Repeat step 2 through 5 until the particle history is terminated due to absorption, escape, or because the particle's emergent phase space coordinates drop below

some arbitrarily specified limit, i.e., energy cut-off, age cut-off, etc.

The above sequence of events is directly applicable to neutron transport, photon transport, and electron transport for electrons with energies greater than an arbitrary cutoff energy used to invoke the continuous energy loss term shown in Eq. 2-6. However, for electrons with energies below the cutoff energy, and for all charged particles, the sequence of events changes to incorporate the continuous energy loss term. More specifically, the collision integral operator defined in Eq. 2-15 is given by:

$$C(\bar{r},E'\to E,\bar{\Omega}'\to\bar{\Omega}) = \int_{I'}^{E_{MAX}} dE' \int d\bar{\Omega}' \frac{\Sigma_s(\bar{r},E'\to E,\bar{\Omega}'\to\bar{\Omega})}{\Sigma_t(\bar{r},E')} + \frac{\frac{\partial}{\partial E}\left[S(E)\right]}{\Sigma_t(\bar{r},E)} , \quad (2\text{-}20)$$

where

I' is an arbitrary value taken to be the minimum energy for which discrete interaction is allowed, and

E_{MAX} is the maximum energy considered.

Interactions involving particles with incident energy less than I' are considered to undergo a continuous slowing down with a fixed energy loss per unit path length traveled. This quantity is referred to as the stopping power and represents an integral over the cross section for the energy range zero to I'. Therefore, when a particle undergoes a continuous slowing down type interaction, the particle suffers only energy degredation and no angular deflection, i.e., straightahead scattering. A complete derivation of the

continuous slowing down equation can be found in Ref. 25 and will not be repeated here.

Implementing the collision integral operator defined in Eq. 2-20 into the random walk sequence is straightforward. The sequence of events described earlier remains the same for steps one through four. Step five was changed to include the continuous energy loss term and the energy ranges over which the two terms in the collision integral operator apply. In particular, step five becomes:

5. If the incident energy of the particle is greater than the cutoff energy I' and an absorption occurs, the sequence is initiated again for a new particle. If a scattering reaction occurs and the incident energy of the particle is greater than the cutoff energy I' a new direction ($\bar{\Omega}_1$) is selected according to the marginal distribution function $\int dE\Sigma_s(\bar{r}_1, E_0 \rightarrow E, \bar{\Omega}_0 \rightarrow \bar{\Omega})/\Sigma_s(\bar{r}_1, E_0)$. A new energy ($E_1$) is determined from the conditional probability distribution function $\Sigma_s(\bar{r}_1, E_0 \rightarrow E, \bar{\Omega}_0 \rightarrow \bar{\Omega}_1)/\Sigma_s(\bar{r}_1, E_0)$. If a scattering reaction occurs and the incident energy of the particle is less than the cutoff energy I', the energy degredation, $E_0 \rightarrow E_1$, is determined from the stopping power S(E) for the distance transported, $r_0 \rightarrow r_1$, and the emergent direction $\bar{\Omega}_1$ is equal to the incident direction $\bar{\Omega}_0$. If the energy degredation is greater than the incident energy of the particle, the particle is assumed to have slowed to rest, i.e., "ranged out," in the medium.

Step six of the sequence remains the same. For electrons, the cutoff energy I′ is arbitrarily set by the user when processing the cross sections. (Typical values for I′ in the present work were set for electron kinetic energies of 0.01 MeV) For charged particles other than electrons, I′ was equal to E_{MAX}. Therefore, for these particles, all collisions were treated with the continuous energy loss term.

An effect of interest such as biological dose, energy deposition, or particle flux for a given problem can be expressed as any one of the following functionals:

$$\lambda = \iiint P^{\phi}(\bar{r},E,\bar{\Omega})\phi(\bar{r},E,\bar{\Omega})\,d\bar{r}\,dE\,d\bar{\Omega} \quad , \tag{2-21}$$

$$\lambda = \iiint P^{\psi}(\bar{\bar{r}},E,\bar{\Omega})\psi(\bar{r},E,\bar{\bar{\Omega}})\,d\bar{r}\,dE\,d\bar{\Omega} \quad , \tag{2-22}$$

or

$$\lambda = \iiint P^{\chi}(\bar{\bar{r}},E,\bar{\Omega})\chi(\bar{r},E,\bar{\bar{\Omega}})\,d\bar{r}\,dE\,d\bar{\Omega} \quad , \tag{2-23}$$

where

$P^{\phi}(\bar{r},E,\bar{\Omega})$ = the response function of the effect of interest due to a unit angular flux $(\bar{r},E,\bar{\Omega})$,

$P^{\psi}(\bar{r},E,\bar{\bar{\Omega}})$ = the response function of the effect of interest due to a particle which experiences an event at $(\bar{\bar{r}},E,\bar{\Omega})$, and

$P^{\chi}(\bar{r},E,\bar{\bar{\Omega}})$ = the response function of the effect of interest due to a particle which emerges from a collision at $\bar{r}$ with phase space coordinates $(\bar{\bar{r}},E,\bar{\bar{\Omega}})$.

The cumulative score from a random walk is the single particle estimate of the effect of interest, λ. The Monte Carlo estimate $\hat{\lambda}$ of the effect of interest λ is obtained by observing the behavior of large numbers of individual radiation particles. More specifically, the Monte Carlo estimate of λ is given by:

$$\hat{\lambda} = \frac{1}{N} \sum_{i=1}^{N} \lambda_i \ , \tag{2-24}$$

where N is the number of random walks analyzed.

From the Law of Large Numbers, if a true value for λ exists, then the estimate $\hat{\lambda}$ will almost always approach λ as $N \to \infty$. Since it is impossible to transport an infinite number of particles, the variance of the Monte Carlo estimate must be computed to indicate the statistical uncertainty of the Monte Carlo estimate, $\hat{\lambda}$. The Monte Carlo estimate of the variance is given by:

$$\sigma^2 = \frac{1}{N-1} \sum_{i=1}^{N} (\lambda_i - \hat{\lambda})^2 \ , \tag{2-25}$$

where N is the number of random walks analyzed. It should be noted that as $N \to \infty, \hat{\lambda} \to \bar{\lambda}$, and

$$\sigma^2 = \underset{N \to \infty}{\text{LIM}} \left[\frac{1}{N} \sum_{i=1}^{N} (\lambda_i - \bar{\lambda})^2 \right]. \tag{2-26}$$

In the Monte Carlo method as applied to radiation transport, the standard deviation of the mean is usually a reliable indicator of the reproducibility of $\hat{\lambda}$. The standard deviation of the mean is given by:

$$\sigma_{\hat{\lambda}} = \left(\frac{\sigma^2}{N}\right)^{\frac{1}{2}} , \tag{2-27}$$

where N is the number of random walks analyzed. From the Central Limit Theorem, there would be a 68% chance that the $\hat{\lambda}$ estimate of $\bar{\lambda}$ would lie within the internal $\bar{\lambda} \pm \sigma_{\bar{\lambda}}$ centered about the true value $\bar{\lambda}$. However, in radiation transport, the true value $\bar{\lambda}$ is generally not known, and therefore, a more useful interpretation is that there would be a 68% chance that the true value $\bar{\lambda}$ would lie within the internal $\hat{\lambda} \pm \sigma_{\bar{\lambda}}$. The Monte Carlo method developed for this work processes batches of particles and obtains batch estimates of the effect of interest. Therefore, the overall Monte Carlo estimate of the effect of interest and its variance are given by:

$$\hat{\lambda} = \frac{1}{NB} \sum_{I=1}^{NB} \lambda_I , \tag{2-28}$$

and

$$\sigma^2_{\bar{\lambda}} = \left(\frac{1}{NB-1}\right)\left[\frac{1}{NB} \sum_{I=1}^{NB} \lambda_I^2 - \hat{\lambda}^2\right] , \tag{2-29}$$

where

λ_I is the batch estimate of the effect of interest, and

NB is the number of batches.

There are many variance reduction techniques available for reducing the statistical uncertainty in the Monte Carlo estimate of λ for a given computational time. These variance reduction tech-

niques include source biasing, survival biasing, Russian roulette, splitting, and exponential transform. These biasing schemes have been routinely employed in most forward Monte Carlo analysis for many years. The primary function of biasing is to encourage individual random walks to achieve phase space coordinates from which low variance producing estimates of the effect of interest can be made. In the present work, the basic programming for these variance reduction techniques was included but untested. Therefore, the particle transport is accomplished using the analog Monte Carlo method.

CHAPTER III

NUCLEAR PROCESSES

3.0 INTRODUCTION

One of the objectives stated in the introduction is to develop a general code system that will eliminate most if not all of the approximations associated with current methods. One avenue of meeting this objective is to utilize all available nuclear data applicable to the ionization chamber response analysis.

3.1 NEUTRON INTERACTIONS

For the neutron transport program this involves utilizing all partial cross sections, angular distributions, and secondary energy distributions currently available in the Evaluated Nuclear Data File - ENDF/B-V as required for the Monte Carlo random walk procedure. The data formats and procedures for processing the ENDF/B-V nuclear data are presented in Ref. 26. The recommended procedures are followed explicitly in the neutron cross section processors to assimilate the data into a format suitable for Monte Carlo analysis. In general, this involves formatting the cross sections into linearly interpolable cross section-energy pairs, formulating the angular distributions into normalized energy dependent cumulative distribution functions, and formulating the secondary energy data into either tabulated probability distribution tables or into a data format suitable for sampling with one of the ENDF/B-V secondary energy distribution functions (Watt spectrum, evaporation spectrum, etc.).

All of the nuclear data in ENDF/B-V are tabulated for the laboratory reference system except the neutron elastic and discrete inelastic scattering angular distributions. These data are tabulated for the center-of-mass reference system because these neutron interactions are isotropic in the center-of-mass system for a wide range of neutron energies. Since the Monte Carlo random walk occurs in the laboratory system, exact angle-energy relationships derived from basic momentum principles and presented in Ref. 27 are used to calculate the emergent neutron energy and direction. In particular, for elastic scattering, the scattering angle in the laboratory system is:

$$\mu_{lab} = \frac{\left(1+A\mu_{cm}\right)}{\left(1+A^2+2A\mu_{cm}\right)^{1/2}} \quad , \tag{3-1}$$

and the emergent neutron energy in the laboratory is:

$$E' = \frac{1}{2} E\left[(1-\alpha)\mu_{cm} + (1+\alpha)\right] \quad , \tag{3-2}$$

where

μ_{cm} = cosine of the scattering angle in the center-of-mass system,

μ_{lab} = cosine of the scattering angle in the laboratory system,

A = the mass of the target nucleus divided by the mass of a neutron,

E = the incident neutron energy in the laboratory system,

E' = the emergent neutron energy in the laboratory system, and

$$\alpha = \left(\frac{A-1}{A+1}\right)^2 .$$

For discrete inelastic scattering, the scattering angle in the laboratory system is given by:

$$\mu_{lab} = \left(\frac{E'_{cm}}{E'}\right)^{\frac{1}{2}} \mu_{cm} + \left(\frac{E}{E'}\right)^{\frac{1}{2}}\left(\frac{1}{A+1}\right) \quad , \tag{3-3}$$

and the emergent neutron energy in the laboratory system is:

$$E' = E'_{cm} + \left[\frac{E+2\mu_{cm}(A+1)(E\,E'_{cm})^{\frac{1}{2}}}{(A+1)^2}\right] \quad . \tag{3-4}$$

In Eqs. 3-3 and 3-4, the emergent neutron energy in the center-of-mass system is needed. This can be determined from:

$$E'_{cm} = \left(\frac{A}{A+1}\right)^2 E + \left(\frac{A}{A+1}\right) Q \quad , \tag{3-5}$$

where

E'_{cm} = the emergent neutron energy in the center-of-mass system, and,

Q = the Q value of the reaction specified in the ENDF/B-V data.

All other terms are the same as those used in the elastic scattering equation. Incorporating the exact angle-energy formulas given by Eqs. 3-1 to 3-5 into the neutron transport program correctly models elastic and discrete inelastic neutron scattering in the laboratory system.

To account for neutron scattering at thermal energies, the free gas model is used since it yields a good approximation to the thermal flux spectrum and can be sampled without tables. The free gas scattering model assumes that the neutrons are transported in a monatomic gas having an isotropic Maxwellian distribution of velocities. To obtain the emergent neutron energy and angle, the three velocity components of the target nucleus are sampled from the Maxwell-Boltzmann distribution:[16]

$$P(V_i) = \left(\frac{A}{2\pi kT}\right)^{1/2} \exp -\left(\frac{AV_i^2}{2kT}\right) \quad , \tag{3-6}$$

where

A = the mass of the target nucleus divided by the mass of a neutron,

k = the Boltzmann constant,

T = the equilibrium temperature (°K) of the target nuclei, and

V_i = the target nucleus velocity component in the ith direction for i = x, y, or z.

The emergent neutron direction is sampled from an isotropic distribution in the center-of-mass system. The emergent neutron energy and direction in the laboratory system is then determined through conservation of energy and momentum.

The emergent neutron parameters for all other reactions treated as scattering type reactions are expressed in terms of post-

collision energy and direction in the laboratory system. These scattering type reactions include the continuum mode of inelastic scattering, (n,2n), (n,3n), (n,fission), and (n,n'x) where x represents a charged particle (proton, alpha particle, etc.). In these reactions, the emergent neutron angle is selected from an ENDF/B-V tabulated angular distribution and the emergent neutron energy is selected from an ENDF/B-V tabulated probability distribution or from an evaporation spectrum except for the (n,fission) reaction which uses an energy dependent Watt spectrum. Because of the structure of ENDF/B-V data, single neutron emission models are used for the (n,2n), (n,3n), and (n,fission) reactions with the weights of the emergent neutrons multiplied by two, three and $\bar{\nu}(E)$, respectively. The parameter, $\bar{\nu}(E)$, is the average number of neutrons produced per fission event tabulated as a function of energy.

All charged particle production via absorption reactions i.e., (n,p), (n,α), (n,d), etc., or inelastic scattering reactions with charged particle emission assume isotropic emission of the charged particle in the laboratory system. The charged particle emergent energy is selected from a general evaporation spectrum given by:[28]

$$F(E \rightarrow E') = \frac{E'}{I} e^{-E'/\theta} \quad , \tag{3-7}$$

where I is a normalization constant dependent on the nuclear temperature (θ) and the emergent particle energy range (E'_{min},E'_{max}) and θ is given by:[28]

$$\theta = 4.016 \times 10^{3} \left[\frac{E_{max}}{A^{5/3}}\right]^{1/2} \quad , \tag{3-8}$$

with $E_{max} = E + Q - CB$ in units of eV. In Eqs. 3-7 and 3-8, E is the incident neutron energy, Q is the ENDF/B-V Q value for the reaction, CB is the Coulomb barrier, A is the mass number in atomic mass units, and E′ is the charged particle exit energy (with the Coulomb barrier added back in). The Coulomb barrier is calculated from:[29]

$$CB = 0.75 \left[\frac{Z_1 Z_2 e^2}{r_1 + r_2} \right] , \tag{3-9}$$

where

Z_1 = the charge number of the recoil heavy ion,

Z_2 = the charge number of the charged particle,

e = the charge of the proton, and

r_1 and r_2 = the atomic radii for the recoil heavy ion and charged particle respectively.

The atomic radius r_i as a function of mass number A_i is given by the following table:

A_i	r_i
$2 \leq A \leq 4$	1.20×10^{-13}
6	2.02×10^{-13}
7	2.43×10^{-13}
8	2.84×10^{-13}
9	3.25×10^{-13}
≥ 10	$1.70\ A_i^{1/3} \times 10^{-13}$

The factor 0.75 is set arbitrarily to account for charged particle emission below the Coulomb barrier.

All compound nuclei excited through neutron interactions (except elastic scattering) possess the potential of emitting one or more photons while decaying to ground state. Therefore, for every neutron interaction except elastic scattering, a check is made to determine if secondary photon production data are available. If there are data available, a photon is produced with a direction assumed isotropic in the laboratory system, an energy selected from the ENDF/B-V tabulated distribution, and weight equal to the ENDF/B-V energy dependent multiplicity. There are some materials with absorption reactions resulting in ground state transitions. For these reactions a test is implemented to insure no secondary photon generation occurs.

The photon production capability is programmed to model the natural physical processes as accurately as possible. Unfortunately, the photon production data in ENDF/B-V are not well known for some of the individual neutron interactions in many materials. Consequently, for these materials, the ENDF/B-V photon production data have been lumped into one file encompassing the individual neutron interactions which might produce a secondary photon. The neutron transport code utilizes these data to produce a photon whose direction, energy, and weight are representative average values for these neutron interactions.

Each neutron interaction produces a recoil heavy ion. In ionization chamber response analysis, recoil heavy ions can deposit energy in the active medium thereby contributing to the detector

signal. Therefore, the energy and direction of the recoil heavy ions must be determined for each neutron interaction. This is accomplished using energy and momentum balances for all incident and exit particles produced in the collision.

3.2 PHOTON INTERACTIONS

The photoelectric effect, Compton scattering and pair production are the three processes considered in the photon transport program. In the photoelectric process, a photon is absorbed and an orbital electron is emitted with approximately all of the energy of the photon transferred to the electron. The electron is ejected from its shell with kinetic energy equal to the incident photon energy less the binding energy of the orbital electron (with a very small amount of energy taken up by the nucleus). Momentum is conserved by recoil of the whole atom. The photoelectric process is the dominant photon interaction for photons with energies below 0.1 MeV. Furthermore, because of momentum and energy conservation considerations, the photoelectric process is more likely to occur with the more tightly bound K-shell and L-shell electrons.

Compton scattering is the elastic scattering of a photon by an essentially free electron. The incident photon imparts energy to the electron and emerges from the collision with a new direction and energy. In the Compton scattering process, the electrons are assumed to be free - that is, not bound within the atom or interacting among themselves. The Compton effect becomes important for incident photon energies greater than 0.1 MeV.

In the pair production process, a photon interacts with the electrostatic field of a charged particle. The incident photon is completely absorbed resulting in the production of an electron-positron pair. This photon interaction requires an incident photon energy of at least twice the rest mass of an electron, i.e., 1.022 MeV, and becomes increasingly more probable as the photon energy increases above 1.022 MeV. Momentum and energy is conserved in the process by the recoil of the charged particle. Either the nucleus or an atomic electron can provide the necessary electrostatic field for the process. Because of the greater charge of the nucleus, the interactions are primarily nuclear. If, however, the process occurs in the field of an atomic electron, energy is transferred to the recoil electron and a triplet is produced.[30] The triplet consists of the recoil electron and the electron-positron pair. Because of momentum and energy considerations, the threshold energy for triplet production is four times the rest mass of an electron, i.e., 2.044 MeV.

The interaction cross sections for the photoelectric, Compton, and pair production processes exhibit a Z dependence.[31] The Compton effect is linearly dependent on the number of electrons per atom and therefore is proportional to Z. The photoelectric process is proportional to Z^n, where n varies from 3 to 5, and diminishes rapidly with increasing photon energy for any element. The pair production process is proportional to Z for interaction with atomic electrons and proportional to Z^2 for interactions with the nucleus. However, only in iron and higher Z materials does the pair production process account for a significant portion of the energy absorption for

incident photon energies below 10 MeV. Consequently, most ionization chamber response analysis for photons will be dominated by the photoelectric and Compton processes. The theoretical and empirical formulae used to generate the cross sections for the above photon interactions are presented in detail in Ref. 19.

3.3 ELECTRON INTERACTIONS

Elastic scattering off the nucleus, inelastic scattering off the atomic electrons, bremsstrahlung production, and positron annihilation are the electron (and positron) interactions considered in the photon transport program. As stated earlier, difficulties arise in electron transport because the cross sections for all the above interactions (except annihilation) become very large as the electron energy approaches zero. Therefore, it is not feasible to simulate every interaction, and they are lumped together and treated in a continuous manner. Cutoff energies are used to distinguish between continuous and discrete interactions. Any electron interaction which produces a delta-ray with an energy greater than the electron cutoff energy or a photon with an energy greater than the photon cutoff energy is considered a discrete event. All other electron interactions are treated in a continuous manner giving rise to continuous energy losses and direction changes to the electron between discrete interactions.

The continuous energy loss models complicate electron transport because the cross section varies along the path of the electron and the electron path is not straight. This complication is rectified by introducing an additional fictitious interaction which forces the

total cross section to remain constant along the electron path. If this fictitious interaction is chosen, the electron experiences a straight-ahead scattering i.e., no interaction at all. Otherwise, the interaction is considered real and is dealt with in the usual manner.

Finally, to account for multiple scattering of the electrons, the transport of the electron between interactions is divided into small steps. Within each small step the electron is assumed to follow a straight line, and multiple scattering is accounted for by changing the electron's direction at the end of each small step. The size of the steps is kept small enough to insure that the true electron path length is not much larger than the straight line path length, and that the angle between the initial and final directions follows the appropriate angular distribution.

The above discussion is condensed from material presented in Ref. 19. As in the case with photon interactions, the theoretical and empirical formulae used to generate the cross sections for the above electron interactions are presented in detail in Ref. 19.

3.4 CHARGED PARTICLE INTERACTIONS

In solving the Boltzmann transport equation for charged particles, i.e., protons, alpha particles, recoil heavy ions, etc., the only interactions considered in the present work are continuous energy loss mechanisms. This is due to the lack of charged particle cross section data for most materials. To simulate a Monte Carlo random walk, a very small fictitious transport cross section is incorporated to determine the next "collision" site. Because this

cross section is very small (1.0×10^{-10}), the charged particle transport kernel will almost always provide the distance to the material boundary as the distance to be transported. Prior to transport, the particle's range for complete energy loss is calculated from the stopping power and range/energy table using the following relation:[32]

$$R(E) = \int_o^E \frac{dE}{dE/dx} \quad , \tag{3-10}$$

where

R(E) = the range of a charged particle in a particular medium with energy dE about E, and,

$\frac{dE}{dx}$ = the stopping power of a particular medium for a charged particle with energy dE about E.

If the particle's range is less than the distance to the material boundary, all the particle's energy is assumed deposited in the material. If the range is greater than the distance to the material boundary, the stopping power and range/energy table are used to determine the fraction of energy deposited in the material and the particle is transported to the material boundary with the remaining energy. This process is repeated until the particle loses all of its energy. The theoretical formulae used in the present work for generating the stopping powers and range/energy tables are given in Ref. 32.

Recombination effects are sometimes a problem in gas or liquid ionization chambers. Recombination results from ionized electrons recombining with charged ions thereby decreasing the charge

collected. If recombination effects are significant, the nonlinearity of the charge collected (Q) is taken into account using Birks' law:[21]

$$\frac{dQ}{dx} \propto \frac{\frac{dE}{dx}}{1+kB\frac{dE}{dx}} \quad , \tag{3-11}$$

where kB is the recombination constant determined experimentally. If kB is zero, the charge collected is proportional to the energy deposited, i.e., $\frac{dQ}{dx} \propto \frac{dE}{dx}$. In the code system, recombination effects are computed for each individual particle when they are determined to be significant. However, in ionization chamber analysis, recombination effects are usually negligible. This formulation for calculating recombination effects was chosen because of the ease of application to the stopping powers and range/energy tables used in the charged particle transport.

CHAPTER IV

SYSTEM VERIFICATION AND RESULTS

4.0 INTRODUCTION

Accomplishment of the first four objectives outlined in Chapter I led to the development of MICAP - A Monte Carlo Ionization Chamber Analysis Package. MICAP is a modular code system designed to calculate the response of an ionization chamber to a mixed neutron and photon radiation environment. Figure 4-1 depicts a flow diagram of the overall calculational procedure employed in MICAP. For this collection of codes, the approach has been to develop a "general" ionization chamber analysis code system, applicable to a wide range of problems, through the use of input arrays and user supplied subroutines. A user's manual for MICAP is given in Ref. 33 complete with sample problems for each module.

Establishing the validity of the nuclear models incorporated into the transport modules of the code system involved implementation of a five part verification program. The verification program included comparing results obtained with existing code systems and comparing with experimental results. Each part of the verification program investigated a particular aspect of the radiation transport processes applicable to ionization chamber analysis. More specifically, the verification program involved:

1. Comparisons with MORSE[17] results to determine validity of neutron transport, secondary photon production, and photon transport processes.

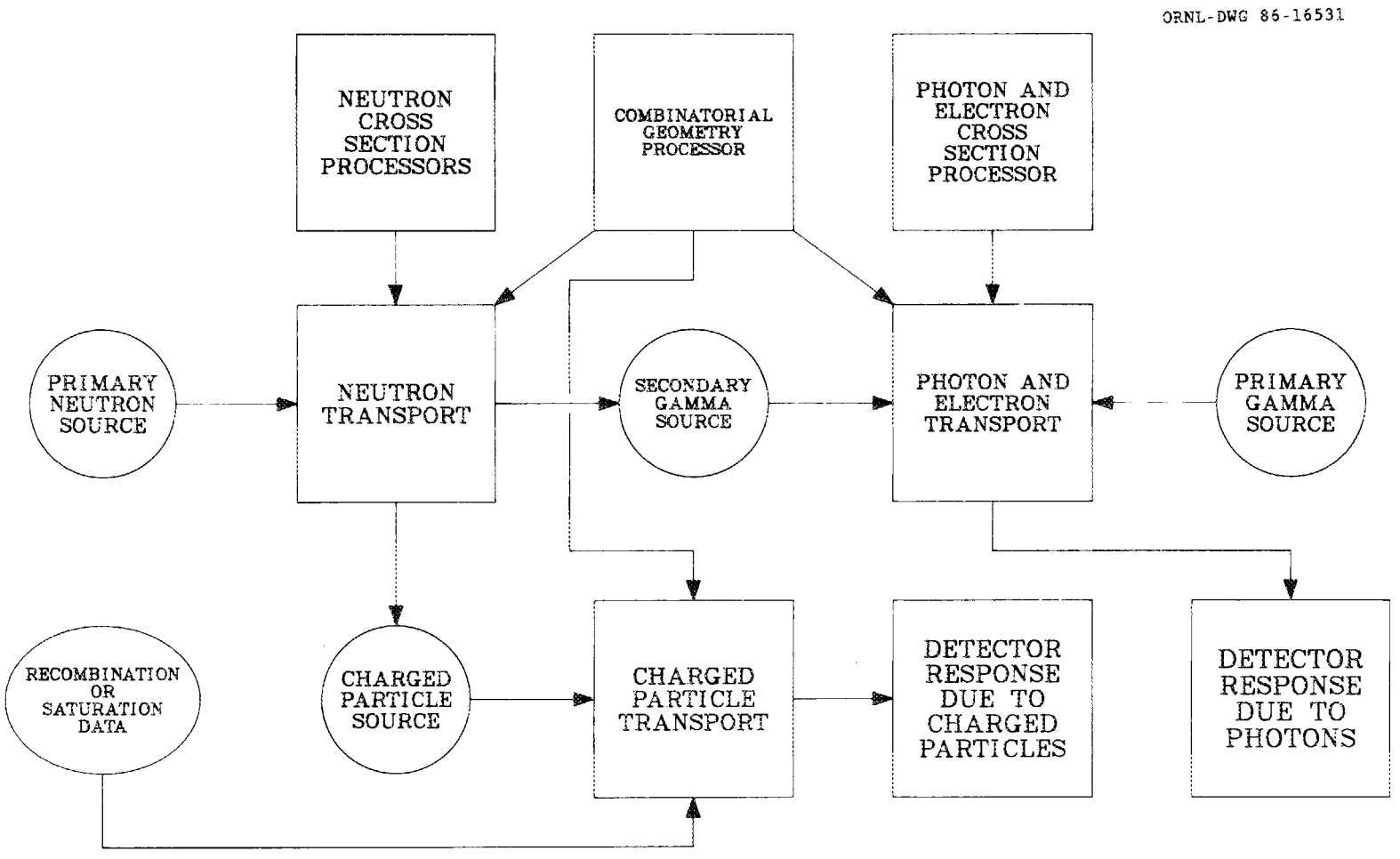

Figure 4-1. Flow Diagram of the Overall Calculational Procedure Employed in MICAP.

2. Comparisons with MACK-IV[34] and RECOIL[35] results to determine validity of nuclear models used to describe individual neutron reactions.
3. Comparisons with O5S[36] results to determine validity of charged particle transport processes.
4. Comparisons with experimental results for photon calibration experiments.
5. Comparisons with experimental results for mixed neutron and photon radiation experiments.

The remainder of this chapter discusses each part of the verification program.

4.1 COMPARISON WITH MORSE

To verify the neutron transport, secondary photon production, and photon transport processes in MICAP, an iron slab transmission problem was analyzed with both MORSE and MICAP. The MORSE code system was chosen for the comparison because its performance has already been verified through comparisons with experiments and comparisons with other code systems.[16,17,37] Consequently, comparisons with MORSE should provide a reliable indication of the validity of the neutron transport, secondary photon production, and photon transport processes in MICAP. The calculations involved modeling a neutron point source incident on the front face of iron slabs having thicknesses 10 and 20 cm. The material parameters for the iron slab are presented in Table 4-1 and the geometry configuration is shown in Figure 4-2. Both code systems calculated the neutron and

Table 4-1. Material Parameters for the Iron Slab

Parameter	Value
Iron	
Chemical formula	Fe
Density	7.870 gm/cm^3
Iron Atom density	8.490×10^{-2} at/b-cm

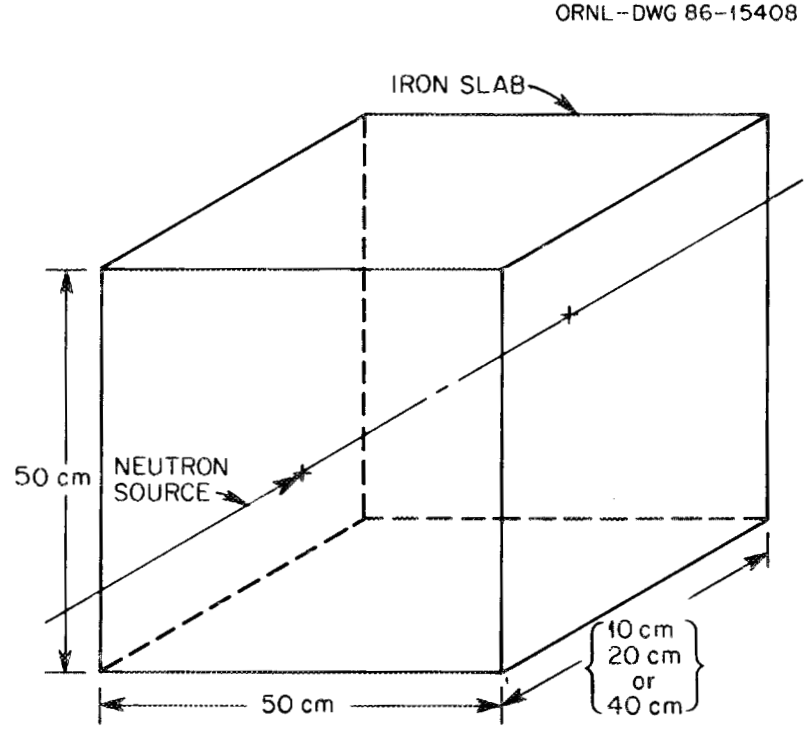

Figure 4-2. Geometry Configuration for the Iron Slab.

secondary photon leakage spectra out the back face of the iron slab, and the secondary photon production in the iron slab.

The iron cross section data used in MICAP differed from those used in the MORSE calculations. MICAP used ENDF/B-V point cross section data thinned to within a tolerance of 0.1%. The MORSE calculations for the 10 cm iron slab used an ENDF/B-IV 105n-21γ coupled, P_3, multigroup library.[18] To insure different cross section data bases were not a source of discrepancy, the MORSE calculations for the 20 cm iron slab used an ENDF/B-V 37n-21γ coupled, P_3, multigroup library[38] as well as the ENDF/B-IV 105n-21γ coupled, P_3, multigroup library.

The 10-cm-thick iron slab was analyzed using a mono-directional point source centered on the front face of the slab and the 20-cm-thick iron slab was analyzed using an isotropic point source centered on the front face. Both iron slabs were analyzed using a ^{238}U fission spectrum neutron source and a mono-energetic neutron source (14.2 MeV for the 10 cm slab and 14.0 MeV for the 20 cm slab). The MORSE calculations used Russian roulette and splitting in the transport and the MICAP calculations were performed using analog Monte Carlo. All calculations used 100,000 source neutrons incident on the iron slab.

The neutron and secondary photon leakage flux spectra out the back face of the 10 cm iron slab and the secondary photon production spectra are presented in Figures 4-3 to 4-5 respectively for the ^{238}U fission neutron source. The figures indicate excellent agreement between MICAP and MORSE for the back face leakage spectra and secondary photon production spectra. The spectral differences seen

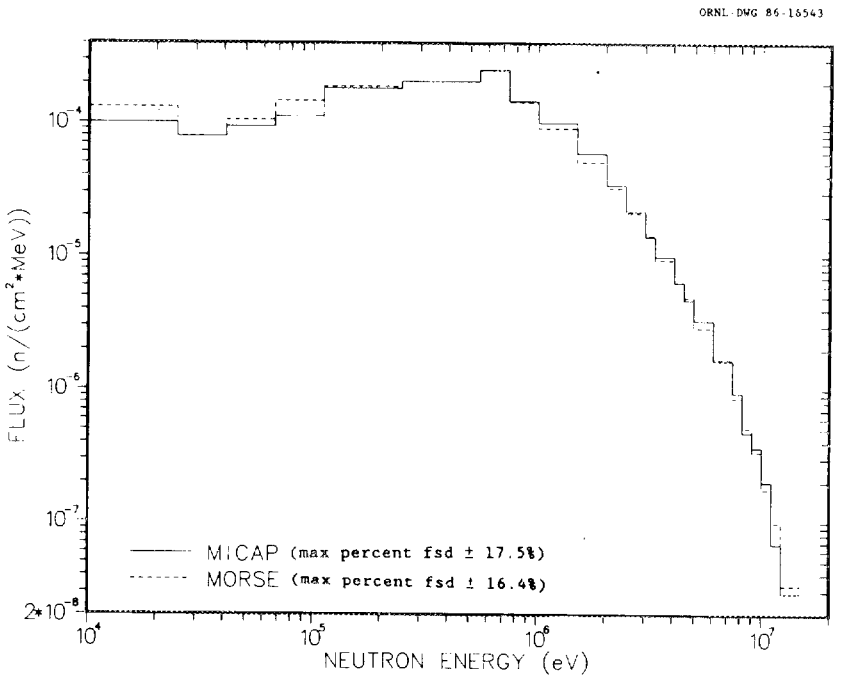

Figure 4-3. Comparison of MICAP and MORSE Neutron Leakage Flux Spectra out the Back Face of a 50 cm x 50 cm x 10 cm Iron Slab with a Point Mono-Directional Fission Neutron Source. (max percent fsd represents maximum percent fractional standard deviation)

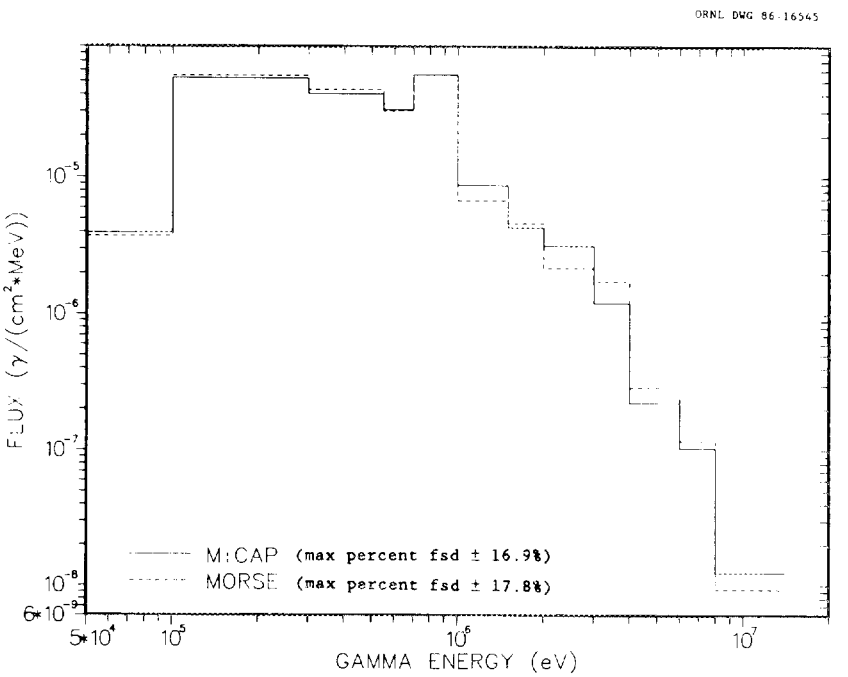

Figure 4-4. Comparison of MICAP and MORSE Photon Leakage Flux Spectra out the Back Face of a 50 cm x 50 cm x 10 cm Iron Slab with a Point Mono-Directional Fission Neutron Source.

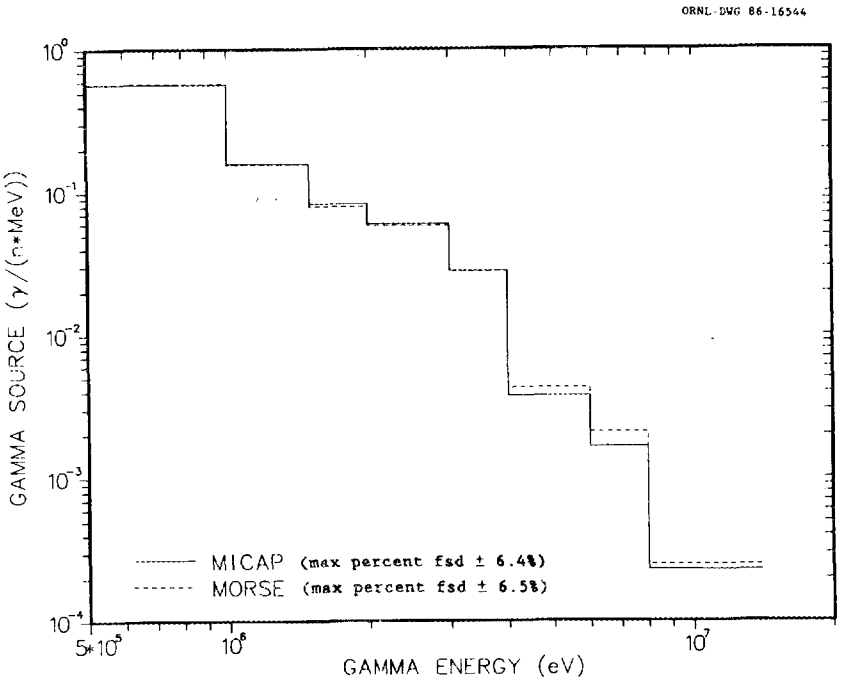

Figure 4-5. Comparison of MICAP and MORSE Secondary Photon Production Spectra in a 50 cm x 50 cm x 10 cm Iron Slab with a Point Mono-Directional Fission Neutron Source.

in Figures 4-3 to 4-5 are within the statistical errors quoted for the two calculations. The statistical errors for the two calculations are unacceptable for benchmarking purposes, however, they do provide a reasonable comparison of the transport processes in MICAP and MORSE. Similar results are shown in the comparison of the MICAP and MORSE neutron and secondary photon leakage flux spectra out the back face of the 20 cm iron slab and the secondary photon production spectra presented in Figures 4-6 to 4-8 for the isotropic 14.0 MeV mono-energetic neutron source. While the results again show spectral differences between MICAP and MORSE, comparisons of the integral quantities presented in Tables 4-2 and 4-3 for the two 10 cm iron slab cases and Tables 4-4 and 4-5 for the two 20 cm iron slab cases show excellent agreement. In Table 4-6, the integral quantities for the MORSE calculations using the ENDF/B-IV and

ENDF/B-V cross section data sets are compared with the MICAP ENDF/B-V results for the 20 cm iron slab and the isotropic 14.0 MeV mono-energetic neutron source. The fission neutron source results were not compared because of significant differences between the two input fission source spectra. The only significant difference between the ENDF/B-IV and ENDF/B-V MORSE results in Table 4-6, is the lower secondary photon production calculated in the MORSE ENDF/B-IV results. The lower secondary photon production consequently yields a lower integral photon leakage flux and current out the back face of the slab. While the integral quantities in Table 4-6 show slight differences between the MORSE ENDF/B-IV results and the MICAP and MORSE ENDF/B-V results, the spectral results (not shown) were comparable and within the statistical errors of the

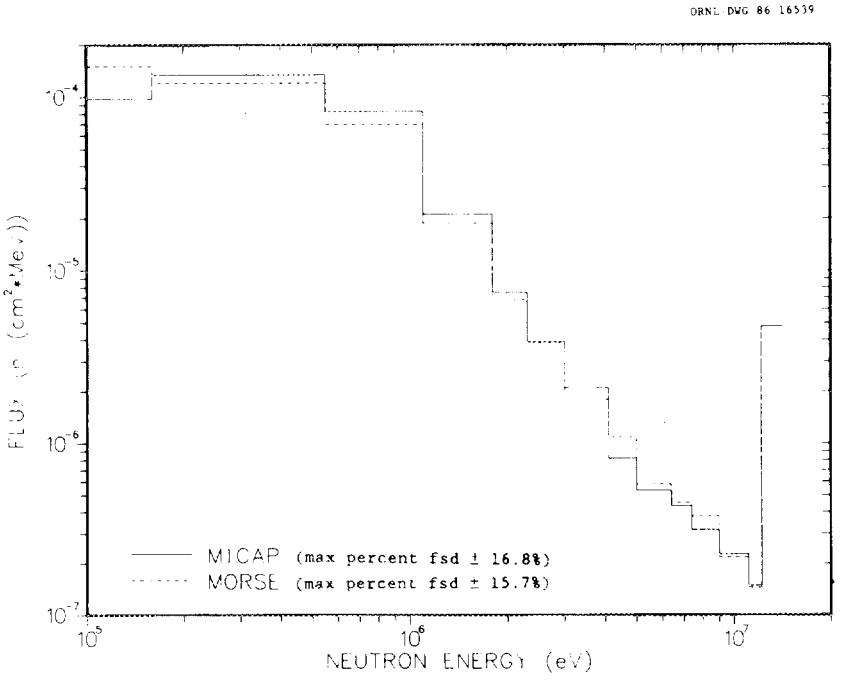

Figure 4-6. Comparison of MICAP and MORSE Neutron Leakage Flux Spectra out the Back Face of a 50 cm x 50 cm x 20 cm Iron Slab with a Point Isotropic 14.0 MeV Neutron Source.

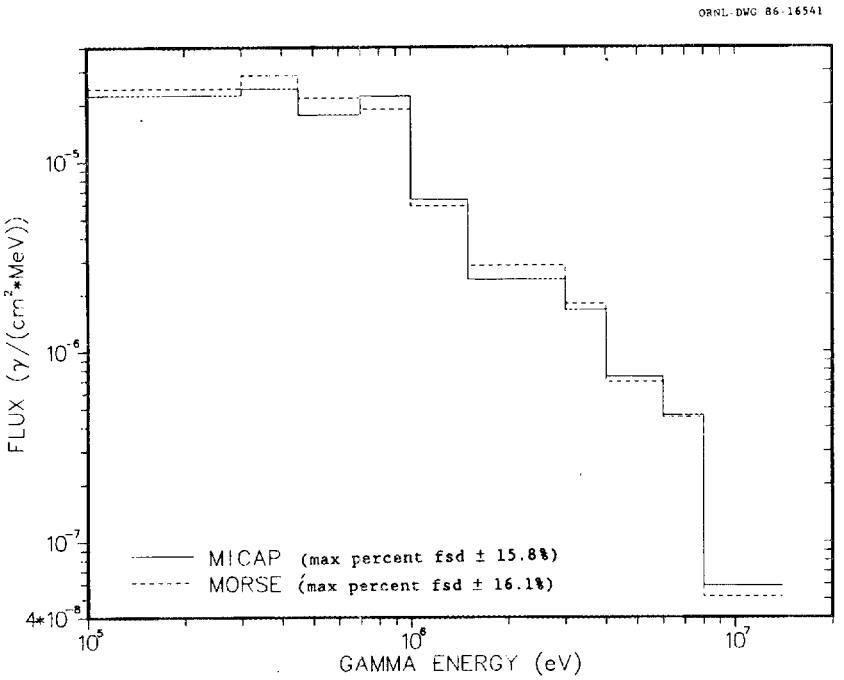

Figure 4-7. Comparison of MICAP and MORSE Photon Leakage Flux Spectra out the Back Face of a 50 cm x 50 cm x 20 cm Iron Slab with a Point Isotropic 14.0 MeV Neutron Source.

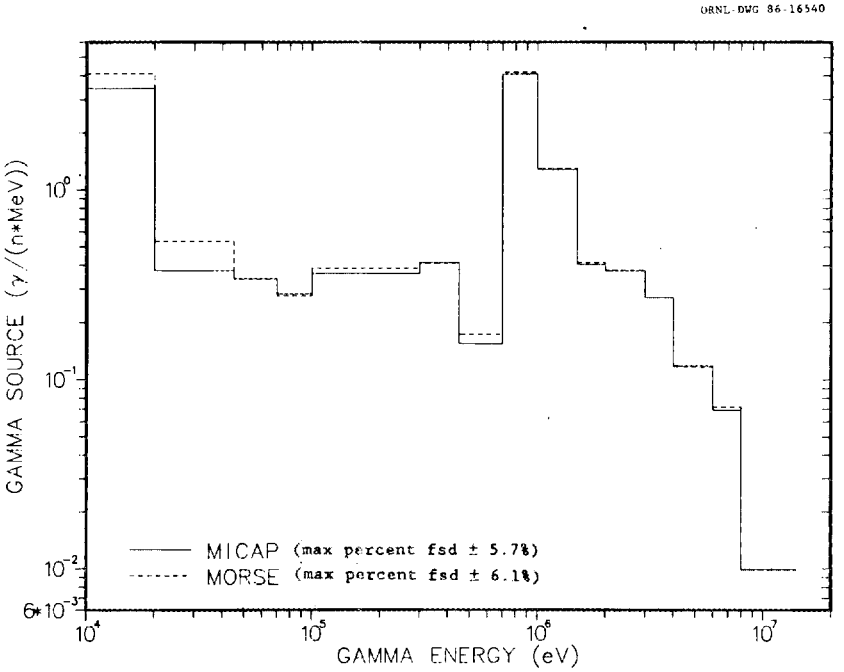

Figure 4-8. Comparison of MICAP and MORSE Secondary Photon Production Spectra in a 50 cm x 50 cm x 20 cm Iron Slab with a Point Isotropic 14.0 MeV Neutron Source.

Table 4-2. Comparison of MICAP and MORSE Integral Quantities for the 50 cm x 50 cm x 10 cm Iron Slab with a Point Mono-Directional Fission Neutron Source

Quantity	MICAP	MORSE
Neutron flux leakage out the back face (n/cm^2)	3.15-04 (0.007)[a]	3.07-04 (0.007)
Neutron current leakage out the back face (n/cm^2)	1.97-04 (0.004)	1.90-04 (0.004)
Secondary photon production (γ/n)	7.85-01 (0.013)	7.89-01 (0.004)
Photon flux leakage out the back face (γ/cm^2)	5.38-05 (0.046)	5.30-05 (0.020)
Photon current leakage out the back face (γ/cm^2)	3.03-05 (0.052)	2.96-05 (0.014)

[a]Fractional standard deviation ($\sigma(\bar{x})/\bar{x}$).

Table 4-3. Comparison of MICAP and MORSE Integral Quantities for the 50 cm x 50 cm x 10 cm Iron Slab with a Point Mono-Directional 14.2 MeV Neutron Source

Quantity	MICAP	MORSE
Neutron flux leakage out the back face (n/cm^2)	3.92-04 (0.007)[a]	3.78-04 (0.007)
Neutron current leakage out the back face (n/cm^2)	2.50-04 (0.004)	2.47-04 (0.004)
Secondary photon production (γ/n)	2.46+00 (0.004)	2.34+00 (0.003)
Photon flux leakage out the back face (γ/cm^2)	2.18-04 (0.015)	1.90-04 (0.014)
Photon current leakage out the back face (γ/cm^2)	1.21-04 (0.011)	1.06-04 (0.010)

[a]Fractional standard deviation ($\sigma(\bar{x})/\bar{x}$).

Table 4-4. Comparison of MICAP and MORSE Integral Quantities for the 50 cm x 50 cm x 20 cm Iron Slab with a Point Isotropic Fission Neutron Source

Quantity	MICAP	MORSE
Neutron flux leakage out the back face (n/cm^2)	1.08-04 (0.013)[a]	9.05-05 (0.014)
Neutron current leakage out the back face (n/cm^2)	6.43-05 (0.008)	5.30-05 (0.005)
Secondary photon production (γ/n)	5.57-01 (0.006)	6.14-01 (0.005)
Photon flux leakage out the back face (γ/cm^2)	4.33-06 (0.058)	4.80-06 (0.046)
Photon current leakage out the back face (γ/cm^2)	2.59-06 (0.051)	2.84-06 (0.040)

[a]Fractional standard deviation ($\sigma(\bar{x})/\bar{x}$).

Table 4-5. Comparison of MICAP and MORSE Integral Quantities for the 50 cm x 50 cm x 20 cm Iron Slab with a Point Isotropic 14.0 MeV Neutron Source

Quantity	MICAP	MORSE
Neutron flux leakage out the back face (n/cm^2)	1.49-04 (0.017)[a]	1.43-04 (0.012)
Neutron current leakage out the back face (n/cm^2)	8.80-05 (0.008)	8.56-05 (0.007)
Secondary photon production (γ/n)	3.36+00 (0.003)	3.43+00 (0.003)
Photon flux leakage out the back face (γ/cm^2)	3.23-05 (0.026)	3.38-05 (0.027)
Photon current leakage out the back face (γ/cm^2)	1.97-05 (0.022)	2.05-05 (0.022)

[a]Fractional standard deviation ($\sigma(\bar{x})/\bar{x}$).

Table 4-6. Comparison of MICAP and MORSE Integral Quantities for the 50 cm x 50 cm x 20 cm Iron Slab with a Point Isotropic 14.0 MeV Neutron Source and using the ENDF/B-IV and ENDF/B-V Cross Section Data Bases

Quantity	MICAP	MORSE	MORSE
Cross section data base	ENDF/B-V	ENDF/B-V	ENDF/B-IV
Neutron flux leakage out the back face (n/cm^2)	1.49-04 (0.017)[a]	1.43-04 (0.012)	1.47-04 (0.015)
Neutron current leakage out the back face (n/cm^2)	8.80-05 (0.008)	8.56-05 (0.007)	8.77-05 (0.009)
Secondary photon production (γ/n)	3.36+00 (0.003)	3.43+00 (0.003)	3.15+00 (0.003)
Photon flux leakage out the back face (γ/cm^2)	3.23-05 (0.026)	3.38-05 (0.027)	3.01-05 (0.029)
Photon current leakage out the back face (γ/cm^2)	1.97-05 (0.022)	2.05-05 (0.022)	1.81-05 (0.023)

[a] Fractional standard deviation ($\sigma(\bar{x})/\bar{x}$).

calculations. Therefore, the different cross section data bases were not considered significantly different for the purposes of the comparison study. The final verification, offered in Figure 4-9, compares the PHOTON module and MORSE secondary photon flux leakage spectra out the back face of the 20 cm iron slab for the isotropic 14.0 mono-energetic neutron source distribution. In this comparison, the secondary photon production source generated in MORSE was transported by both MORSE and the PHOTON module of MICAP. Once again, Figure 4-9 shows that the spectral differences are within the statistical error. These differences were evidenced in all four calculations; however, comparisons of the integral quantities in Table 4-7 show good agreement for all cases. Based on these comparisons and the fact that MORSE is considered a viable code,

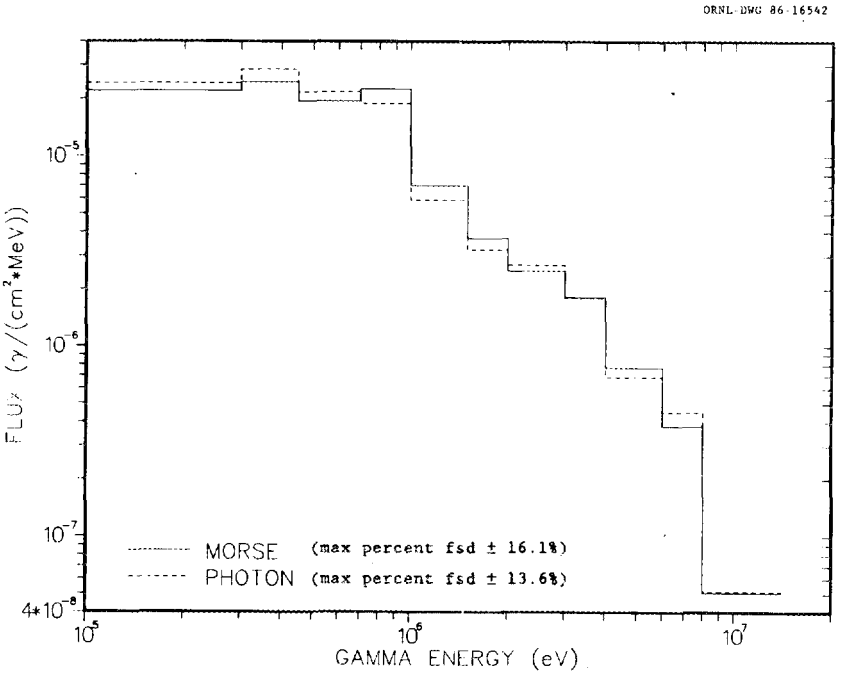

Figure 4-9. Comparison of PHOTON and MORSE Photon Leakage Flux Spectra out the Back Face of a 50 cm x 50 cm x 20 cm Iron Slab with a Point Isotropic 14.0 MeV Neutron Source using the MORSE Generated Secondary Photon Production Data.

Table 4-7. Comparison of PHOTON and MORSE Integral Photon Leakage out the Back Face of the Iron Slab Using the MORSE Generated Secondary Photon Production Data

Iron Slab Calculation (Thickness/Neutron Source)	Photon Flux (γ/cm^2) MORSE	PHOTON	Photon Current (γ/cm^2) MORSE	PHOTON
10 cm/mono-directional fission	5.30-05 (0.020)[a]	5.37-05 (0.018)	2.96-05 (0.014)	3.00-05 (0.014)
10 cm/mono-directional 14.2 MeV	1.90-04 (0.014)	1.98-04 (0.012)	1.06-04 (0.010)	1.11-04 (0.009)
20 cm/isotropic fission	4.80-06 (0.046)	5.49-06 (0.052)	2.84-06 (0.040)	3.13-06 (0.033)
20 cm/isotropic 14.0 MeV	3.38-05 (0.027)	3.39-05 (0.027)	2.05-05 (0.022)	2.06-05 (0.022)

[a] Fractional standard deviation ($\sigma(\bar{x})/\bar{x}$).

the neutron transport, secondary photon production, and photon transport processes in MICAP are considered valid.

4.2 COMPARISON WITH MACK-IV AND RECOIL

The neutron and photon leakage flux spectra and secondary photon production spectra presented in the last section demonstrated the validity of the radiation transport processes. The comparisons, however, did not verify all aspects of the nuclear models used to describe the individual neutron reactions important to ionization chamber response analysis. More specifically, verification is needed for the nuclear models describing the energy transfer from the neutron to the reaction products for all partial cross sections used in MICAP. To accomplish this goal, a problem consisting of a mono-directional 14.2 MeV mono-energetic neutron source incident on a 40-cm-thick iron slab was calculated using MICAP. The material parameters and geometry configuration were the same as that used in the spectral comparisons. The MICAP calculation used 200,000 source neutrons and set an energy cut-off at 14.2 MeV to only allow single collisions. The 40-cm-thickness of iron (several mean-free-paths) insured an adequate number of source interactions in the slab. The charged particles and recoil heavy ions produced in the NEUTRON module were processed in the HEAVY module to determine the average kinetic energies of the charged particles and recoil heavy ions produced by the individual neutron reaction types. The average kinetic energies calculated in program HEAVY were then multiplied by the appropriate cross sections (at 14.2 MeV) to obtain the kerma factors

for the individual neutron reactions. These average kinetic energies and kerma factors were then compared to results obtained with MACK-IV[34] and RECOIL.[35]

The kerma factor comparisons involve using microscopic cross section data evaluated at 14.2 MeV. Because MACK-IV and RECOIL use ENDF/B-IV cross section data and MICAP uses ENDF/B-V cross section data, the microscopic cross sections for the individual neutron reactions used in all three programs are presented in Table 4-8. As seen in Table 4-8, there are considerable differences in some of the cross sections. The cross section differences between MACK-IV and MICAP are attributed to differences in the cross section data bases (ENDF/B-IV versus ENDF/B-V) and to the energy weighting models used to create the MACK-IV multigroup cross section set. The differences between MACK-IV and RECOIL are primarily attributed to differences in cross section processing models.

The results of the average kinetic energy and kerma factor calculations performed in MICAP show good agreement with results from MACK-IV and RECOIL. The comparison with MACK-IV (Table 4-9) lumps the recoil nucleus and charged particle results for a particular reaction together whereas the comparison with RECOIL (Table 4-10) excludes the charged particle results entirely. In viewing Tables 4-9 and 4-10, the effects of the cross section data base are evident in the kerma factor comparisons. In Table 4-9 for instance, the average kinetic energies for the (n,γ) reaction are almost equivalent, but the kerma factors are different by a factor of four. A check of the cross section data in Table 4-8 shows a factor of four difference in the MACK-IV value and MICAP value. Similar

Table 4-8. Iron Microscopic Cross Sections (at 14.2 MeV) Used in the MICAP, MACK-IV, and RECOIL Kerma Factor Calculations

Cross Section (b)	RECOIL	MACK-IV	MICAP
Total	2.54+00	2.57+00	2.57+00
Elastic	1.16+00	1.17+00	1.23+00
(n,2n)	4.57-01	4.32-01	4.23-01
(n,n'α)	3.67-03	1.99-03	2.88-03
(n,n'p)	4.13-02	3.40-02	4.05-02
(n,n') resolved	1.16-01	1.17-01	1.11-01
(n,n') continuum	6.01-01	6.32-01	5.96-01
(n,γ)	2.08-04	2.10-04	8.10-04
(n,p)	1.01-01	1.25-01	1.22-01
(n,d)	1.90-02	1.89-02	6.74-03
(n,t)	4.80-04	1.34-04	6.38-06
(n,^{3}He)	3.50-04	1.30-04	6.38-07
(n,α)	3.92-02	3.98-02	3.94-02

Table 4-9. Comparison of MICAP and MACK-IV Average Kinetic Energies ($\bar{E}$) and Kerma Factors for the Partial Reactions at 14.2 MeV

Reaction	MACK-IV $\bar{E}$ (ev)	MICAP $\bar{E}$ (eV)	MACK-IV Kerma Factor (b-eV)	MICAP Kerma Factor (b-eV)
Total	1.25+06	1.16+06 (0.002)[c]	3.21+06	2.99+06
Elastic	1.05+05	1.08+05 (0.003)	1.23+05	1.33+05
(n,2n)	3.45+05	2.82+05 (0.006)	1.49+05	1.19+05
(n,n' charged particle)[a]	2.77+06	2.58+06 (0.021)	9.96+04	1.12+05
(n,n') resolved	3.62+05	3.63+05 (0.011)	4.21+04	4.04+04
(n,n') continuum	3.24+05	3.39+05 (0.005)	2.05+05	2.02+05
(n,γ)	2.58+05	2.52+05 (0.117)	5.42+01	2.04+02
(n,charged particle)[a]	1.41+07	1.42+07 (0.060)	2.59+06[b]	2.38+06

[a] Recoil nucleus and charged particle included.

[b] Kerma factor = $\Sigma_i \sigma_i (E_n + Q_i)$; for reactions (n,p), (n,t), (n,^{3}He), (n,α).

[c] Fractional standard deviation ($\sigma(\bar{x})/\bar{x}$).

Table 4-10. Comparison of MICAP and RECOIL Average Kinetic Energies ($\bar{E}$) and Kerma Factors for the Partial Reactions at 14.2 MeV

Reaction	RECOIL $\bar{E}$ (eV)	MICAP $\bar{E}$ (eV)	RECOIL Kerma Factor (b-eV)	MICAP Kerma Factor (b-eV)
Total	2.24+05	2.28+05 (0.002)[b]	5.69+05	5.86+05
Elastic	1.09+05	1.08+05 (0.003)	1.26+05	1.33+05
(n,2n)	2.68+05	2.82+05 (0.006)	1.23+05	1.19+05
(n,n'α)[a]	4.28+05	5.92+05 (0.069)	1.57+03	1.70+03
(n,n'p)[a]	2.69+05	3.19+05 (0.019)	1.11+04	1.29+04
(n,n') resolved	3.66+05	3.63+05 (0.011)	4.25+04	4.04+04
(n,n') continuum	3.31+05	3.39+05 (0.005)	1.99+05	2.02+05
(n,γ)	2.52+05	2.52+05 (0.117)	5.24+01	2.04+02
(n,p)[a]	3.42+05	3.40+05 (0.010)	3.45+04	4.13+04
(n,d)[a]	3.55+05	4.03+05 (0.040)	6.75+03	2.71+03
(n,t)[a]	3.28+05	3.93+05 (0.258)	1.57+02	2.50+00
(n,^{3}He)[a]	3.88+05	4.05+05 (0.240)	1.36+02	2.58-01
(n,α)[a]	6.31+05	8.49+05 (0.018)	2.47+04	3.34+04

[a] Exit charge particle not included.

[b] Fractional standard deviation ($\sigma(\bar{x})/\bar{x}$).

results are seen in Table 4-10. In general, the nuclear models used in MICAP to describe the individual neutron reactions are adequate for calculating ionization chamber responses. The principal differences noted above are due to different cross section data bases and cross section processing techniques.

4.3 COMPARISON WITH O5S

In the last section, verification of the nuclear models used to describe the individual neutron reactions was described. In essence, this procedure verified the charged particle and recoil heavy ion source generation processes in program NEUTRON in much the same way as the comparisons to MORSE verified the secondary photon production processes. The charged particle and recoil heavy ion transport processes in program HEAVY, however, remain to be verified. To accomplish this task, a comparison to O5S[36] was made. O5S is a specialized Monte Carlo code for calculating pulse height distributions due to mono-energetic neutrons incident on organic scintillators. O5S is specialized in that the code handles only carbon-hydrogen organic compounds and models only right circular cylinders. O5S is further restricted in the carbon and hydrogen neutron reactions which are allowed to occur. Even with the above restrictions, O5S has been used extensively to calculate pulse height distributions for calibration experiments with mono-energetic neutrons. A comparison of pulse height distributions calculated in O5S and MICAP would therefore verify the charged particle and recoil heavy ion transport models in program HEAVY.

The calculations involved modeling a mono-directional 14.2 MeV mono-energetic neutron source distributed over the face of a polyvinyltoluene (grade BC501) plastic scintillator. The material parameters for BC501 are presented in Table 4-11 and the source and geometry configuration are presented in Figure 4-10. O5S is different from typical Monte Carlo programs in that the number of source neutrons undergoing at least one collision is input rather than the total number of source particles tracked. O5S then tracks source particles until the required number have undergone at least one collision. To obtain adequate statistics for the pulse height distribution comparison (fsd's less than ± 10%), approximately 60,000 individual source particles undergoing at least one collision were considered sufficient. Therefore both O5S and MICAP processed approximately 170,000 incident source neutrons.

The comparison of the pulse height distributions generated in O5S and MICAP is presented graphically in Figure 4-11. Both distributions are normalized to 60,000 contributing source particles and plotted as functions of energy in cobalt units. One cobalt unit is the base-line intercept of a straight line fit to the high end of a ^{60}Co gamma ray pulse height distribution.[36] The comparison in

Table 4-11. Material Parameters for the BC501 Polyvinyltoluene Plastic Scintillator

Parameter	Value
Polyvinyltoluene	
Chemical formula	$CH_{1.287}$
Density	0.900 gm/cm^3
Carbon atom density	4.079×10^{-2} at/b-cm
Hydrogen atom density	5.250×10^{-2} at/b-cm

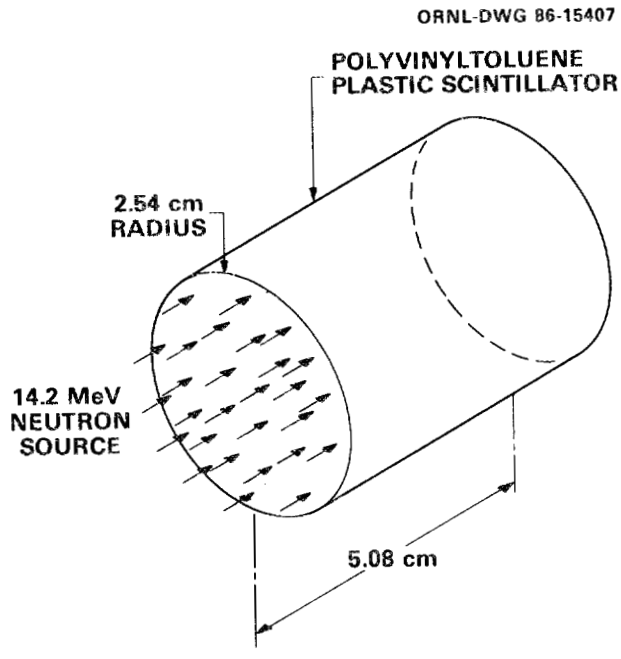

Figure 4-10. Geometry Configuration for the BC501 Polyvinyltoluene Plastic Scintillator.

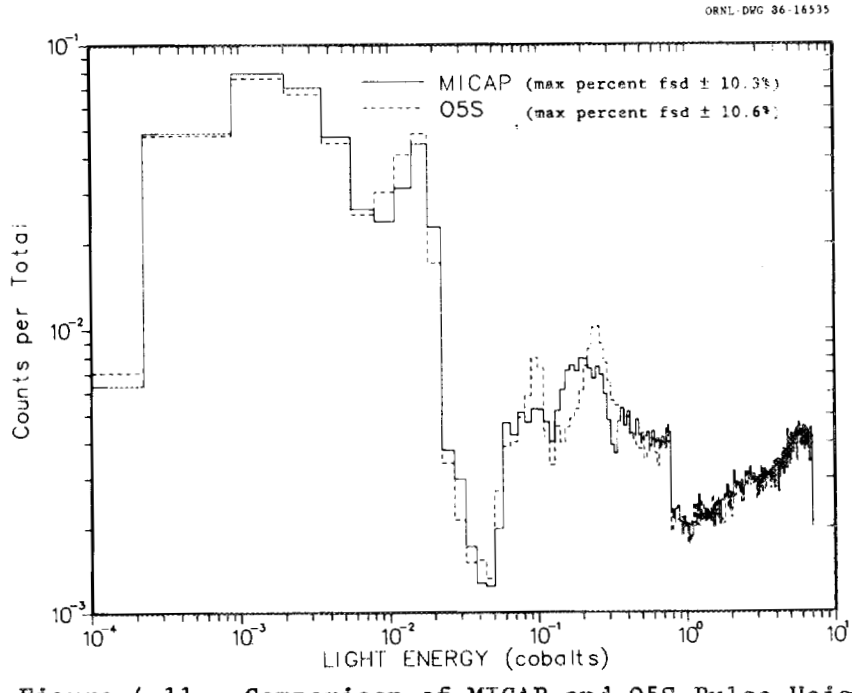

Figure 4-11. Comparison of MICAP and O5S Pulse Height Distributions for a BC501 Polyvinyltoluene Plastic Scintillator with a Mono-Directional 14.2 MeV Neutron Source.

Figure 4-11 shows excellent agreement between O5S and MICAP. Three distinct contributions can be seen in the pulse height distributions presented in Figure 4-11, with each contribution dominated by a different particle type. The low energy contribution (below 4×10^{-2} cobalts) is due primarily to carbon recoil, the intermediate energy contribution (between 4×10^{-2} and approximately 8×10^{-1} cobalts) is due primarily to alpha particle recoil, and the high energy contribution (above approximately 8×10^{-1} cobalts) is due primarily to proton recoil. These contributions were plotted separately in Figures 4-12 to 4-14 to show better resolution. The carbon recoil (Figure 4-12) and proton recoil pulse heights (Figure 4-14) agree to within the statistics of the Monte Carlo calculations. The alpha particle recoil pulse heights (Figure 4-13) however, reflect differences in the models employed in the two programs.

The two neutron reactions generating the alpha particle recoil pulse height are the $^{12}C(n,n'3\alpha)$ and the $^{12}C(n,\alpha)$ reactions. In viewing Figure 4-13, the pulse height for O5S contains two distinct peaks at approximately 1.0×10^{-1} and 2.5×10^{-1} cobalts and a small peak at approximately 7.5×10^{-1} cobalts. The two large peaks are produced by alpha particles generated from the $^{12}C(n,n'3\alpha)$ reaction and the small peak is produced by alpha particles generated from the $^{12}C(n,\alpha)$ reaction. The two large distinct peaks result from the O5S treatment of $^{12}C(n,n'3\alpha)$ collisions. Carbon contains eighteen discrete levels of inelastic scattering capable of decaying to ground state via three alpha particle emission. To simplify programming and save core storage space, O5S allows only the three most probable levels to occur. Two of these levels occur 95% of the time

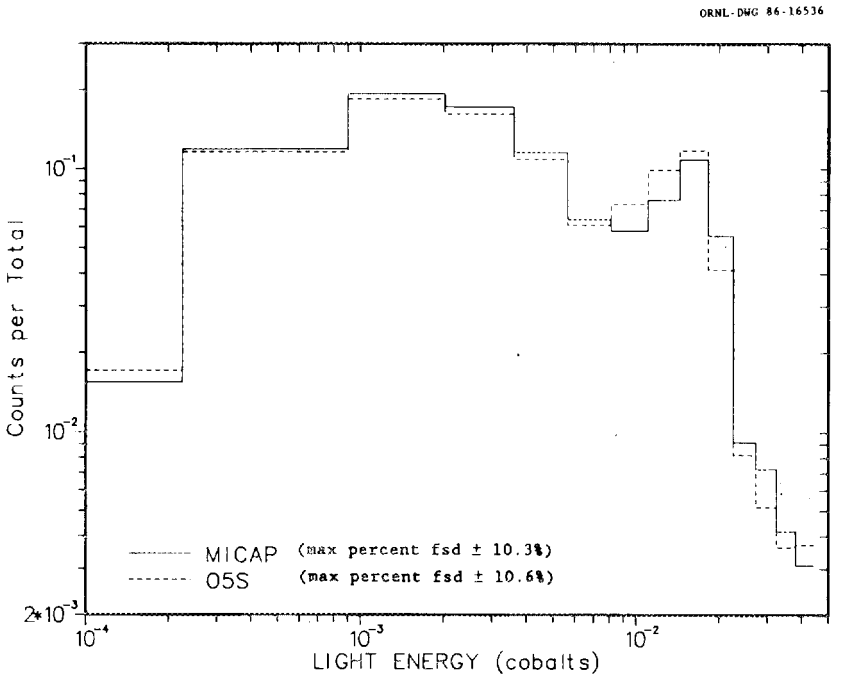

Figure 4-12. Comparison of MICAP and O5S Pulse Height Distributions due Predominantly to Carbon Recoil for a BC501 Polyvinyltoluene Plastic Scintillator with a Mono-Directional 14.2 MeV Neutron Source.

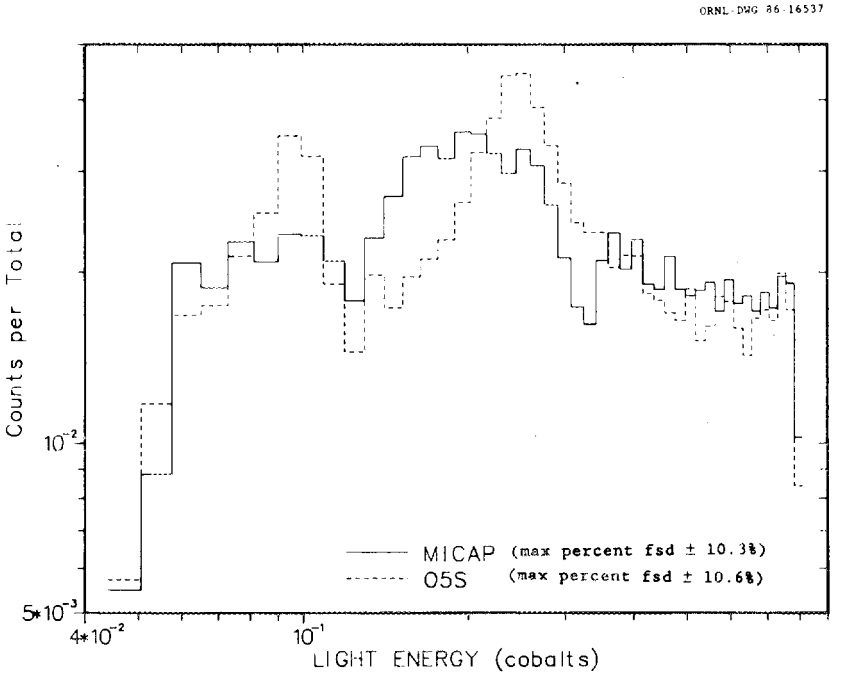

Figure 4-13. Comparison of MICAP and O5S Pulse Height Distributions due Predominantly to Alpha Recoil for a BC501 Polyvinyltoluene Plastic Scintillator with a Mono-Directional 14.2 MeV Neutron Source.

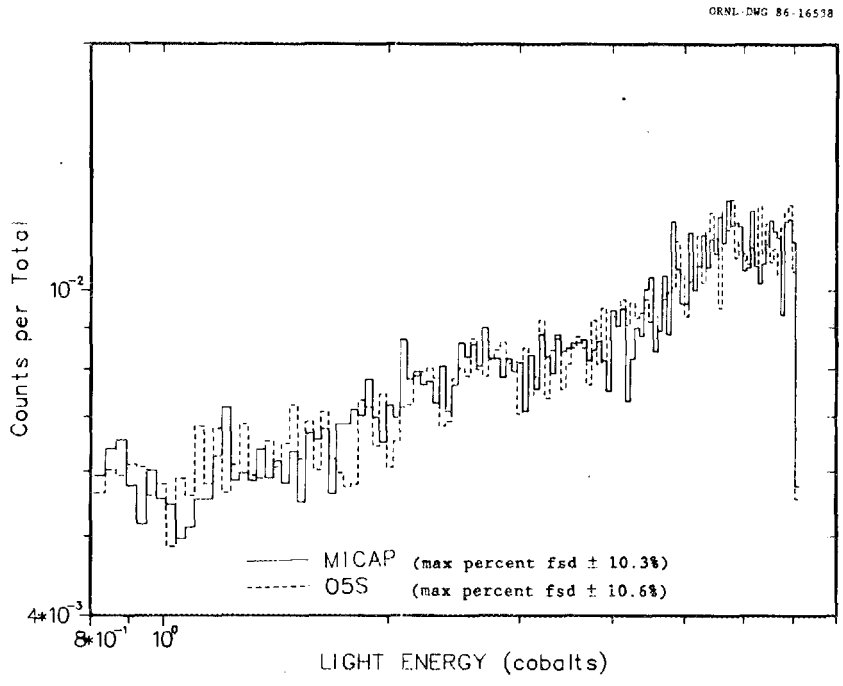

Figure 4-14. Comparison of MICAP and 05S Pulse Height Distributions due Predominantly to Proton Recoil for a BC501 Polyvinyltoluene Plastic Scintillator with a Mono-Directional 14.2 MeV Neutron Source.

(in 05S) and correspond to the two distinct peaks shown in Figure 4-13. MICAP maintains all discrete levels of inelastic scattering data and therefore generates much broader peaks in the alpha particle pulse height distribution as seen in Figure 4-13. The MICAP pulse height distribution is considered a more accurate representation of the true pulse height distribution. While the spectral shapes in the alpha particle pulse height are different, the integral contributions are in excellent agreement.

Additional comparisons between 05S and MICAP were made on the zero bias efficiency (defined as the number of source particles undergoing at least one collision divided by the total number of source particles) and on the average number of collisions per colliding neutron. 05S calculated a zero bias efficiency of 0.37 and 1.41 collisions/colliding neutron. The MICAP results were in excel-

lent agreement with a zero bias efficiency of 0.36 and 1.46 collisions/colliding neutrons. Even though MICAP required more execution time, (6 minutes cpu for MICAP versus 1 minute cpu for O5S on an IBM 3033) the more detailed nuclear models and the non-restricted application capability of MICAP make it a viable detector analysis code system.

4.4 COMPARISON WITH PHOTON CALIBRATION EXPERIMENTS

The preceding comparisons with existing codes have demonstrated the various components of the radiation transport processes important in ionization chamber response analysis. To demonstrate the ability of using the general Monte Carlo code system MICAP to calculate ionization chamber response functions, two mono-energetic photon calibration experiments were analyzed. The first experiment calculated was the Health and Safety Laboratory (HASL) calibration experiment of the high pressure argon ionization chamber systems used in the measurement of environmental radiation exposure rates.[39] The material properties for the HASL high pressure argon chamber are presented in Table 4-12 and the geometry model is presented in Figure 4-15. The second experiment calculated was the Armed Forces Radiobiology Research Institute (AFRRI) ^{60}Co calibrations of their ionization chambers performed at AFRRI and the National Bureau of Standards (NBS).[40-42] The AFRRI ionization chambers include the graphite/carbon dioxide (C/CO_2) and tissue-equivalent plastic/tissue equivalent gas (TE/TE) 50 cm^3 chambers, the magnesium/argon (MG/AR) and (TE/TE) 0.5 cm^3 chambers, and the (TE/TE) 0.05 cm^3 chamber. The material properties for the AFRRI ionization chambers are presented

Table 4-12. Material Parameters for the Health and Safety Laboratory (HASL) High Pressure Argon Ionization Chamber

Parameter	Value
Aluminum	
Chemical formula	Al
Density	2.699 g/cm^3
Aluminum atom density	6.027×10^{-2} at/b-cm
Porcelain	
Chemical formula	Al_2O_3 2 SiO_2
Density	2.600 gm/cm^3
Aluminum atom density	1.410×10^{-2} at/b-cm
Oxygen atom density	4.935×10^{-2} at/b-cm
Silicon atom density	1.410×10^{-2} at/b-cm
Stainless Steel 304	
Chemical formula	0.74 Fe + 0.18 Cr + 0.08 Ni
Density	7.930 gm/cm^3
Iron atom density	6.331×10^{-2} at/b-cm
Chromium atom density	1.654×10^{-2} at/b-cm
Nickel atom density	6.510×10^{-3} at/b-cm
Air @ 1 Atm	
Chemical formula	0.756 N + 0.232 O + 0.013 Ar
Density	1.292×10^{-3} g/cm^3
Nitrogen atom density	4.203×10^{-5} at/b-cm
Oxygen atom density	1.128×10^{-5} at/b-cm
Argon atom density	2.503×10^{-7} at/b-cm
Argon gas	
Chemical formula	Ar
Density @ 9.2 atm	1.639×10^{-2} gm/cm^3
Argon atom density @ 9.2 atm	2.472×10^{-4} at/b-cm
Density @ 21.7 atm	3.867×10^{-2} gm/cm^3
Argon atom density @ 21.7 atm	5.832×10^{-4} at/b-cm
Density @ 36.8 atm	6.557×10^{-2} gm/cm^3
Argon atom density @ 36.8 atm	9.890×10^{-4} at/b-cm

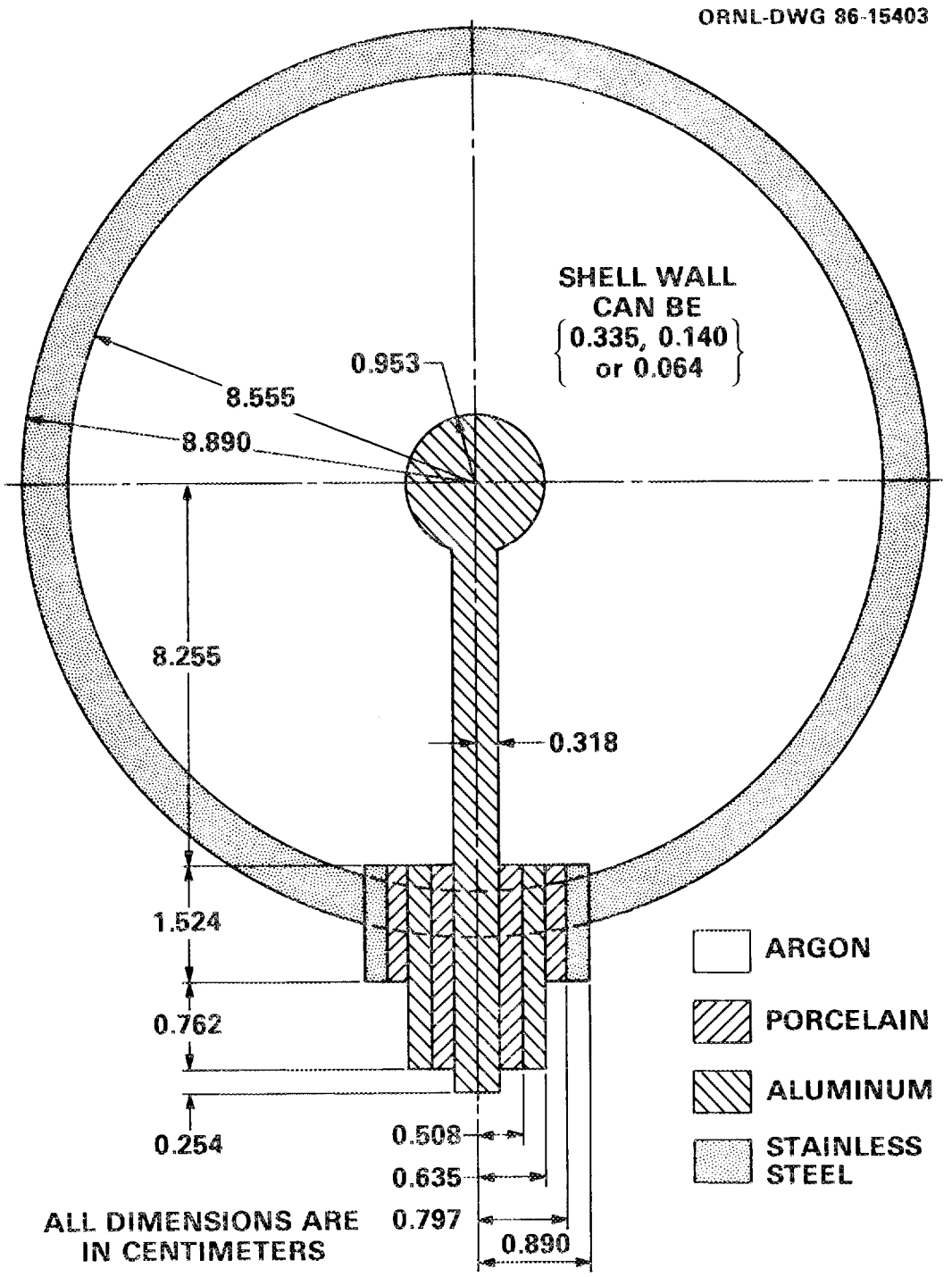

Figure 4-15. Geometry Configuration for the Health and Safety Laboratory (HASL) High Pressure Argon Ionization Chamber.

in Table 4-13 and the geometry models for the 50 cm^3, 0.5 cm^3, and 0.05 cm^3 chambers are shown in Figures 4-16, 4-17, and 4-18 respectively. Both sets of experiments placed the ionization chamber in a collimated beam of mono-energetic photons and measured the amount of charge collected (which is proportional to the energy deposited in the gas). The experiments were positioned such that background effects from the experimental rooms were negligible.

The calculations modeled the ionization chambers presented in Figures 4-15 to 4-18 exactly using combinatorial geometry. The input included the geometry description and two problem dependent subprograms. The first subprogram modeled the input source distribution generated in program PHOTPREP with respect to position, energy, and direction. The second subprogram initialized the photon transport program PHOTON, calculated and integrated the energy deposited in the cavity by each contributing particle, and integrated the results to obtain the total energy deposited in the cavity. This quantity was then normalized to the incident source strength and compared to the experimental values. The electron, positron, and photon cross section data were generated by the PECSP module of MICAP using the material data in Tables 4-12 and 4-13.

The comparison of the MICAP and experimental results are shown in Table 4-14 for the HASL calibration experiments. The MICAP calculations analyzed 50,000 to 300,000 incident source particles depending on the argon gas pressure and incident photon source energy. As seen in Table 4-14, the calculated-to-experimental ratios (C/E) show excellent agreement for almost all cases. The calculations agreed to within 10% of the experimental values in all

Table 4-13. Material Parameters for the Armed Forces Radiobiology Research Institute (AFRRI) Ionization Chambers

Parameter	Value
Aluminum	
Chemical formula	Al
Density	2.699 gm/cm^3
Aluminum atom density	6.027×10^{-2} at/b-cm
Argon gas @ 1 Atm	
Chemical formula	Ar
Density	1.783×10^{-3} gm/cm^3
Argon atom density	2.690×10^{-5} at/b-cm
Graphite	
Chemical formula	C
Density	1.710 gm/cm^3
Carbon atom density	8.578×10^{-2} at/b-cm
Magnesium	
Chemical formula	Mg
Density	1.740 gm/cm^3
Magnesium atom density	4.312×10^{-2} at/b-cm
Polystyrene	
Chemical formula	CH
Density	1.060 gm/cm^3
Carbon atom density	4.905×10^{-2} at/b-cm
Hydrogen atom density	4.905×10^{-2} at/b-cm
Teflon	
Chemical formula	C_2F_4
Density	2.200 gm/cm^3
Carbon atom density	2.650×10^{-2} at/b-cm
Fluorine number density	5.301×10^{-2} at/b-cm
Polyethylene	
Chemical formula	CH_2
Density	0.920 gm/cm^3
Carbon atom density	3.952×10^{-2} at/b-cm
Hydrogen atom density	7.903×10^{-2} at/b-cm
Brass	
Chemical formula	0.70 Cu + 0.30 Zn
Density	8.522 gm/cm^3
Copper atom density	5.656×10^{-2} at/b-cm
Zinc atom density	2.356×10^{-2} at/b-cm

Table 4-13. (continued)

Parameter	Value
Lucite	
Chemical formula	$C_5H_8O_2$
Density	1.200 gm/cm^3
Hydrogen atom density	5.777×10^{-2} at/b-cm
Carbon atom density	3.611×10^{-2} at/b-cm
Oxygen atom density	1.444×10^{-2} at/b-cm
Micarta	
Chemical formula	$C_{12}H_{10}O_2$
Density	1.300 gm/cm^3
Hydrogen atom density	4.206×10^{-2} at/b-cm
Carbon atom density	5.047×10^{-2} at/b-cm
Oxygen atom density	8.412×10^{-3} at/b-cm
Carbon Dioxide @ 1 Atm	
Chemical formula	CO_2
Density	1.965×10^{-3} gm/cm^3
Carbon atom density	2.690×10^{-5} at/b-cm
Oxygen atom density	5.380×10^{-5} at/b-cm
Air @ 1 Atm	
Chemical formula	0.756 N + 0.232 O + 0.013 Ar
Density	1.292×10^{-3} gm/cm^3
Nitrogen atom density	4.203×10^{-5} at/b-cm
Oxygen atom density	1.128×10^{-5} at/b-cm
Argon atom density	2.503×10^{-7} at/b-cm
Tissue Equivalent Gas @ 1 Atm	
Chemical formula	0.644 CH_4 + 0.324 CO_2 + 0.032 N_2
Density	1.138×10^{-3} gm/cm^3
Hydrogen atom density	6.937×10^{-5} at/b-cm
Carbon atom density	2.602×10^{-5} at/b-cm
Nitrogen atom density	1.713×10^{-6} at/b-cm
Oxygen atom density	1.744×10^{-5} at/b-cm
Tissue Equivalent Plastic A-150	
Chemical formula	0.102H + 0.768 C + 0.059 O + 0.036 N + 0.018 Ca + 0.017 F
Density	1.127 gm/cm^3
Hydrogen atom density	6.871×10^{-2} at/b-cm
Carbon atom density	4.342×10^{-2} at/b-cm
Nitrogen atom density	1.745×10^{-3} at/b-cm
Oxygen atom density	2.504×10^{-3} at/b-cm
Fluorine atom density	6.076×10^{-4} at/b-cm
Calcium number density	3.049×10^{-4} at/b-cm

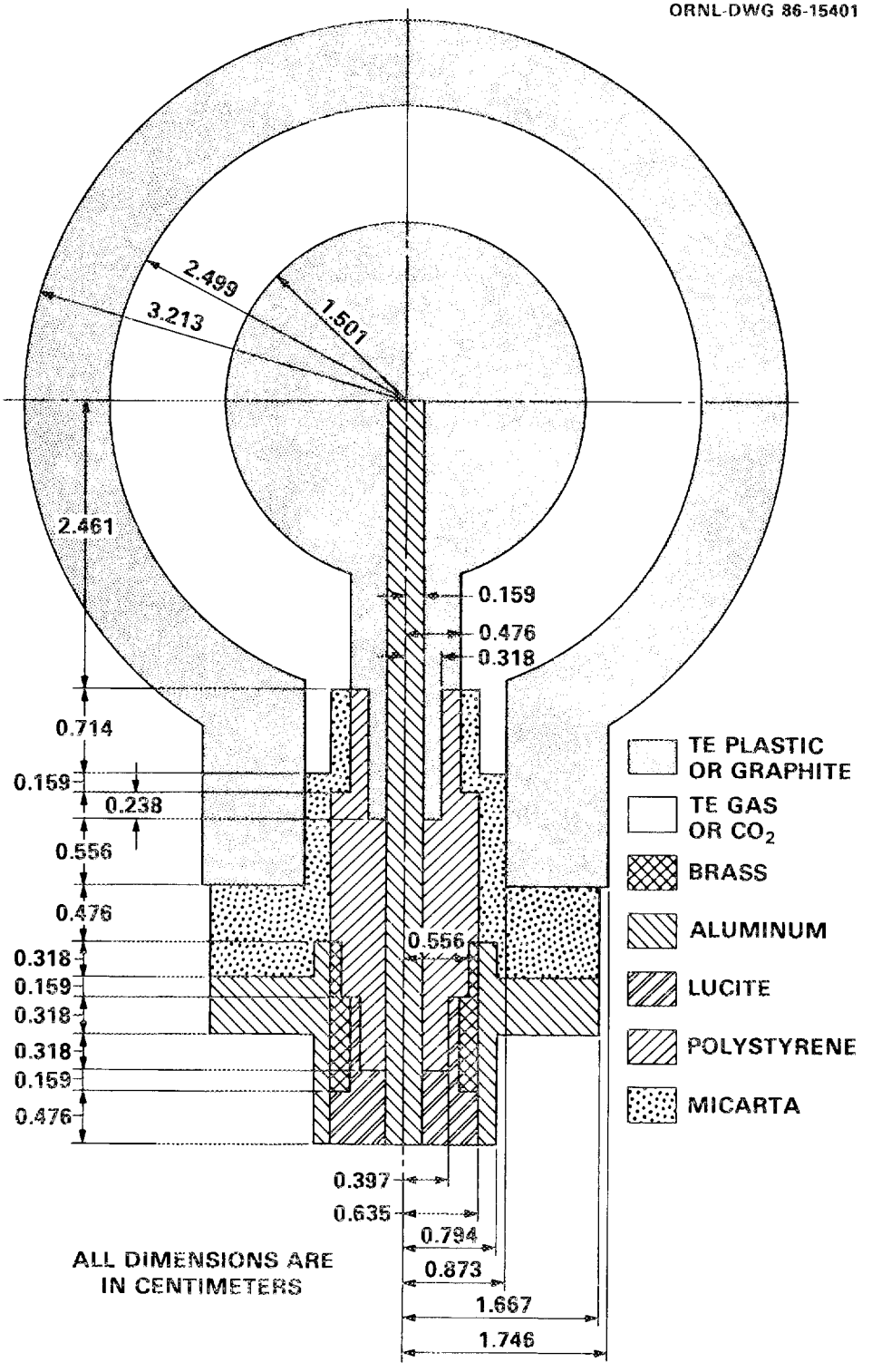

Figure 4-16. Geometry Configuration for the Armed Forces Radiobiology Research Institute (AFRRI) 50 cm^3 Ionization Chamber.

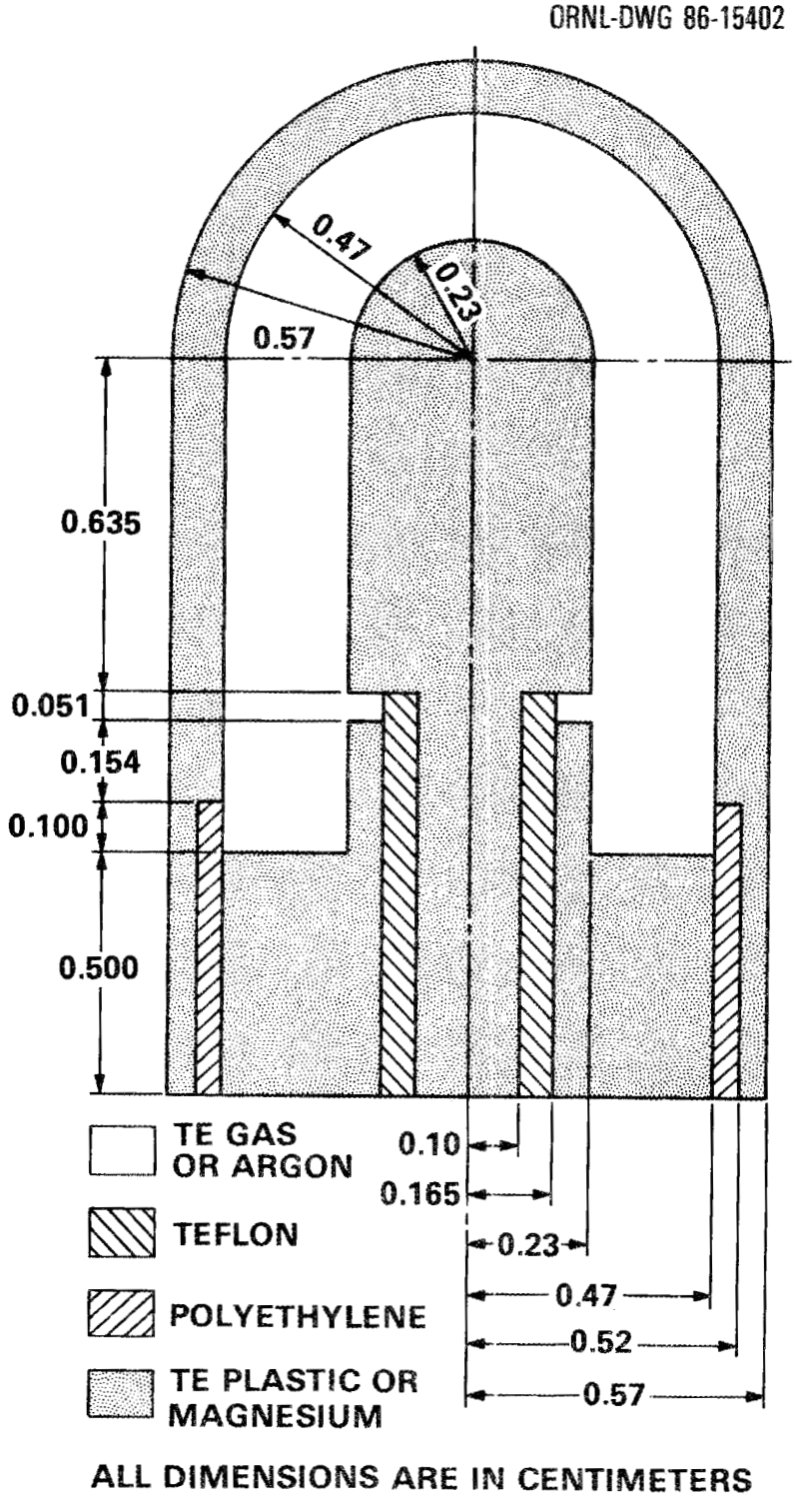

Figure 4-17. Geometry Configuration for the Armed Forces Radiobiology Research Institute (AFRRI) 0.5 cm^3 Ionization Chamber.

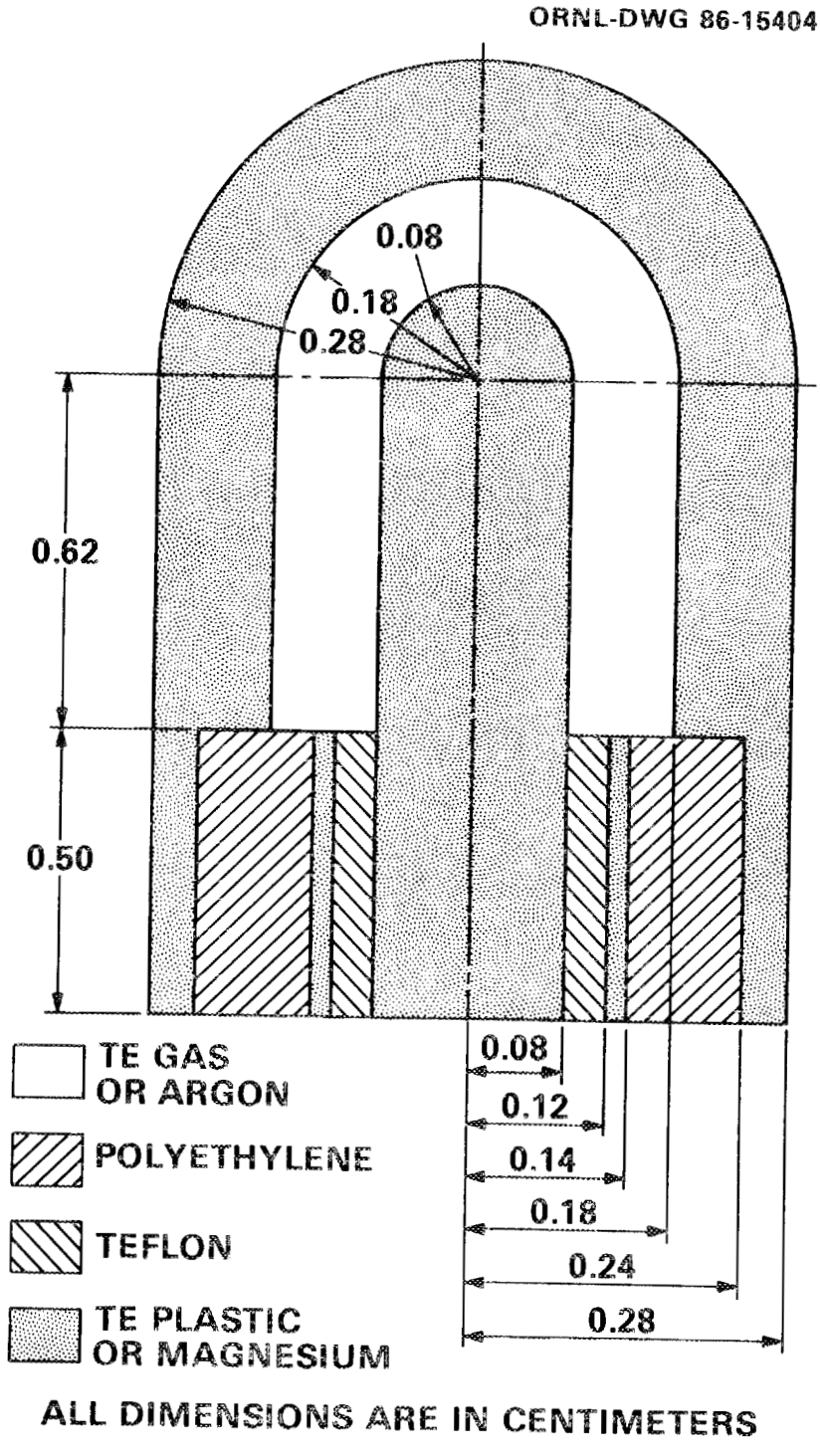

Figure 4-18. Geometry Configuration for the Armed Forces Radiobiology Research Institute (AFRRI) 0.05 cm^3 Ionization Chamber.

Table 4-14. Comparison of Measured and Calculated Detector Responses for the Photon Calibration Experiments of the Health and Safety Laboratory (HASL) High Pressure Argon Ionization Chamber

Photon Source	Source Energy (MeV)	Detector Pressure (Atm)	Calculated Response ($A/\mu R\text{-}hr^{-1}$ ($x10^{-15}$))	Measured[a] Response ($A/\mu R\text{-}hr^{-1}$ ($x10^{-15}$))	C/E
^{241}Am	0.06	9.2	20.2 (0.021)[b]	20.3	0.995
^{141}Cs	0.145	9.2	6.63 (0.023)	7.86	0.844
^{137}Cs	0.662	9.2	3.86 (0.024)	4.03	0.958
^{60}Co	1.25	9.2	3.89 (0.023)	4.00	0.973
^{241}Am	0.06	21.7	20.3 (0.021)	21.9	0.928
^{141}Cs	0.145	21.7	14.1 (0.020)	15.4	0.916
^{137}Cs	0.662	21.7	8.57 (0.022)	8.78	0.976
^{60}Co	1.25	21.7	8.85 (0.023)	9.46	0.936
^{241}Am	0.06	36.8	4.05 (0.022)	4.92	0.823
^{141}Cs	0.145	36.8	18.1 (0.021)	19.3	0.938
^{137}Cs	0.662	36.8	12.3 (0.022)	12.8	0.961
^{60}Co	1.25	36.8	13.1 (0.023)	13.2	0.992

[a] Experimental uncertainty
± 4% for ^{60}Co source
± 5% for ^{141}Cs and ^{137}Cs sources
± 7% for ^{241}Am source

[b] Fractional standard deviation $(\sigma(\bar{x})/\bar{x})$.

but two cases, which involved low energy photon sources. No explanation could be found as to why these two cases do not agree as well as the other cases. The discrepancy for these two cases could be partially due to an error in the experiment (within the experimental procedure itself or in the recording of the data). Furthermore, the consistent underestimation of the experimental response by the MICAP calculations is not understood at this time.

The comparisons of the MICAP and experimental results for the AFRRI 50 cm^3 ionization chambers are presented in Table 4-15 and the comparisons of the MICAP and experimental results for the AFRRI 0.5 cm^3 and 0.05 cm^3 ionization chambers are presented in Table 4-16. The comparisons of calculated and experimental results for the 50 cm^3 ionization chambers show excellent agreement in Table 4-15. The calculations analyzed 500,000 source particles incident on the detector. The calculated-to-experimental ratios (C/E) are well within 10% for all cases analyzed. The results also show a systematic overestimation for the C/CO_2 chamber and underestimation for the TE/TE chamber. As in the HASL study, the exact cause is not known. A sensitivity study was performed however, on the TE/TE and C/CO_2 chambers with 0.72 cm wall thickness. Both chambers were evaluated for a ±10% change in gas density and the C/CO_2 chamber was evaluated for a ±5% change in graphite density. The effect of gas density was significant in the sensitivity calculations. For the TE/TE chamber, the C/E ratio was 0.902 for a -10% change in gas density and 1.08 for a +10% change. Likewise, for the C/CO_2 chamber, the C/E ratio was 0.877 for a -10% change in gas density and 1.09 for a +10% change. Therefore, an error in the gas density

Table 4-15. Comparison of Measured and Calculated Detector Responses for the Photon Calibration Experiments of the Armed Forces Radiobiology Research Institute (AFRRI) 50 cm^3 Ionization Chambers

Photon Source	Source Energy (MeV)	Detector Type	Wall Thickness (cm)	Calculated Response (pA)	Measured[a] Response (pA)	C/E
^{60}Co	1.25	C/CO_2	0.72	179 (0.017)[b]	173	1.04
^{60}Co	1.25	C/CO_2	1.10	172 (0.021)	171	1.01
^{60}Co	1.25	C/CO_2	1.38	182 (0.021)	170	1.07
^{60}Co	1.25	C/CO_2	1.66	174 (0.023)	168	1.04
^{60}Co	1.25	TE/TE	0.72	123 (0.017)	127	0.969
^{60}Co	1.25	TE/TE	1.02	121 (0.018)	125	0.968
^{60}Co	1.25	TE/TE	1.34	117 (0.023)	124	0.944
^{60}Co	1.25	TE/TE	1.67	120 (0.023)	123	0.976

[a] Experimental uncertainty ± 1%.

[b] Fractional standard deviation $(\sigma(\bar{x})/\bar{x})$.

Table 4-16. Comparison of Measured and Calculated Detector Responses for the Photon Calibration Experiments of the Armed Forces Radiobiology Research Institute (AFRRI) 0.5 cm^3 and 0.05 cm^3 Ionization Chambers

Photon Source	Source Energy (MeV)	Detector Type (Buildup cap)	Detector Volume (cm^3)	Calculated Response (pA)	Measured[a] Response (pA)	C/E
^{60}Co	1.25	TE/TE	0.5	0.91 (0.035)[b]	1.29	0.705
^{60}Co	1.25	Mg/Ar	0.5	1.70 (0.030)	1.98	0.859
^{60}Co	1.25	TE/TE (2mm)	0.5	281. (0.033)	311.	0.904
^{60}Co	1.25	Mg/Ar (2mm)	0.5	401. (0.037)	394.	1.02
^{60}Co	1.25	TE/TE (4mm)	0.5	229. (0.031)	270.	0.848
^{60}Co	1.25	TE/TE (4mm)	0.05	17.6 (0.022)	26.0	0.677

[a] Experimental uncertainty
± 5% for 0.5 cm^3 chambers
± 10% for 0.05 cm^3 chambers.

[b] Fractional standard deviation ($\sigma(\bar{x})/\bar{x}$).

calculations will result in comparable errors in the calculated results. The graphite wall density effects were found to be less significant. The sensitivity study yielded a C/E ratio of 1.03 for a -5% change in graphite density, and 0.99 for a +5% change. Therefore, a slight error in graphite density will cause a lessor error in the calculated response. For the problems analyzed, this error was within the statistical error of the Monte Carlo calculations.

The results of the 0.5 cm^3 and 0.05 cm^3 calculations vary when compared to experiment. As seen in Table 4-16, the C/E ratios range from 0.677 to 1.02 for the different cases analyzed. Each chamber was analyzed with 900,000 source particles incident on the chamber wall material. Overall, the results indicate several trends in the calculational ability of MICAP with respect to ionization chamber size. First, MICAP appears to have difficulty reproducing the smaller chamber results. This is evidenced by the 0.05 cm^3 TE/TE C/E ratio of 0.677 and the 0.5 cm^3 TE/TE chamber (with no build-up cap) C/E ratio of 0.705. Variations in wall thickness (nominally 0.1 cm) could partly be responsible for these discrepancies; however, confirmation would require detailed sensitivity calculations. A second trend is the larger C/E ratios for the smaller measured signals. This could possibly be due to errors in the experimental results. It should be noted that this same trend is apparent in the experimental uncertainty presented at the bottom of Table 4-16.

One final result which contributes to the explanation of the discrepancy between calculated and experimental results is seen in the ^{60}Co pulse height distribution for the 50 cm^3 TE/TE ionization chamber shown in Figure 4-19. This curve is representative of the

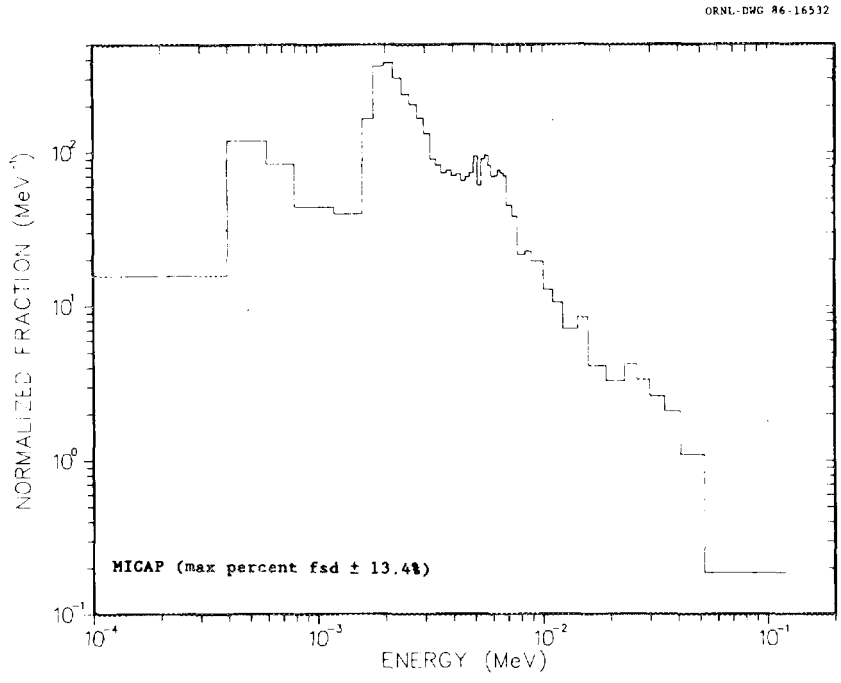

Figure 4-19. Pulse Height Distribution for the Armed Forces Radiobiology Research Institute (AFRRI) TE/TE 50 cm^3 Ionization Chamber due to a Mono-Directional ^{60}Co Photon Source.

pulse height distributions for the ionization chambers analyzed and shows a broad distribution as a function of energy. Furthermore, the pulse height contains a long high-energy tail which affects the calculation of the average energy deposited per source particle. Although the fractional standard deviation for the Monte Carlo result in Table 4-15 was approximately ±2%, the tail of the pulse height distribution could be undersampled and therefore lead to an inaccurate calculated value.

The results of the photon calibration experiment comparisons show the applicability of MICAP to ionization chamber response calculations even though the AFRRI small chamber results were inconclusive. The ultimate and final evaluation of MICAP is made with the mixed-field results presented in the next section.

4.5 COMPARISON WITH MIXED FIELD EXPERIMENTS

The results presented in the preceding section demonstrated the ability of MICAP to calculate ionization chamber response functions for mono-energetic photon calibration experiments. Although this verification is necessary, the real benefit of MICAP is for mixed field experiments. To demonstrate the ability of using MICAP to calculate ionization chamber response functions for mixed neutron and photon radiation environments, three radiation experiments were analyzed.[42-43] The first experiment analyzed was performed at the NBS ^{252}Cf facility. This experiment involved exposing the 50 cm^3 and 0.5 cm^3 ionization chambers individually, in free air, at a nominal distance of 30 cm from the center of the ^{252}Cf source. The source and detector were positioned such that room effects were negligible. The second and third experiments were performed at the AFRRI TRIGA reactor described in Ref. 44. These experiments were performed in exposure room 1 (ER1) of the reactor facility for two of the most frequently used reactor configurations:

1. Bare room with no shielding placed between the experiment and the reactor core (ER1 Free Field), and
2. 15 cm lead shield placed in front of the reactor tank wall to attenuate photons (ER1 15 cm Pb).

The AFRRI experiments exposed a pair of ionization chambers about 10 cm apart and approximately 100 cm from the reactor core center. The experimental setup for the bare room (ER1 Free Field) is shown in Figure 4-20 and for the 15 cm lead shield (ER1 15 cm Pb) in Figure 4-21. The two ionization chambers exposed were the 0.5 cm^3 TE/TE

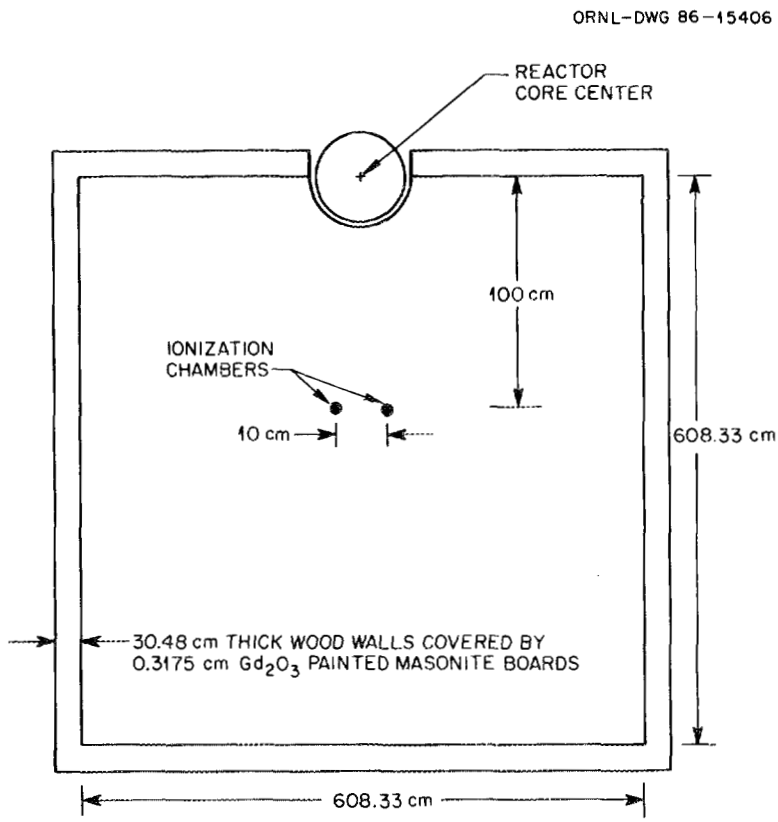

Figure 4-20. Schematic Top View of the Armed Forces Radiobiology Research Institute (AFRRI) Experimental Room One Free Field (ER1 FF) Experiment.

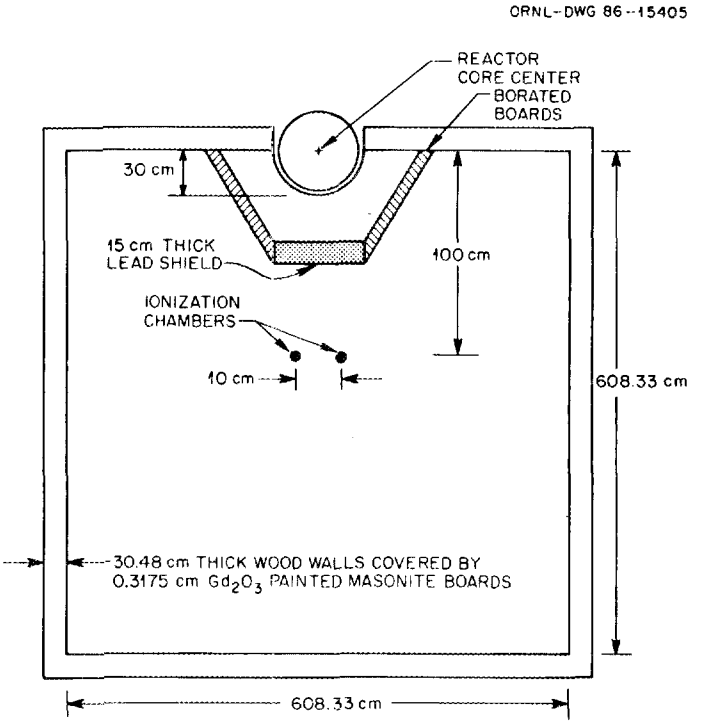

Figure 4-21. Schematic Top View of the Armed Forces Radiobiology Research Institute (AFRRI) Experimental Room One 15 cm Lead Shield (ER1 15 cm Pb) Experiment.

ionization chamber and the 0.5 cm^3 Mg/Ar ionization chamber. As in the NBS ^{252}Cf experiment, the room effects were negligible.

The calculations modeled the ionization chambers exactly using combinatorial geometry. The material properties and geometry description for the AFRRI chambers are given in the last section in Table 4-13 and Figures 4-16 and 4-17. The primary neutron and photon spectra for the AFRRI exposure room experiments (at the detector position) are given in Tables 4-17 and 4-18 respectively. These spectra were obtained from Ref. 45. The NBS ^{252}Cf spectra (also presented in Tables 4-17 and 4-18) were obtained from Refs. 42 and 46. The neutron source spectra (Table 4-17) was input to the NEUTRON program and the recoil heavy ion and secondary photon production sources were generated for subsequent transport in program

Table 4-17. Primary Neutron Source Spectra Used in the Armed Forces Radiobiology Research Institute (AFRRI) Mixed Neutron and Photon Radiation Field Ionization Chamber Calculations

Group Number	Neutron Energy (eV)	ER1* Free Field	ER1* 15 cm Lead	^{252}Cf* Source
1	1.96+07	4.95-06	2.14-06	1.62-05
2	1.69+07	2.25-05	9.42-06	5.88-05
3	1.49+07	2.12-05	8.59-06	4.94-05
4	1.42+07	1.52-05	6.00-06	4.12-05
5	1.38+07	8.80-05	3.46-05	1.71-04
6	1.28+07	7.79-05	3.00-05	1.76-04
7	1.22+07	3.13-04	1.19-04	5.92-04
8	1.11+07	6.68-04	2.55-04	1.26-03
9	1.00+07	1.25-03	4.73-04	2.19-03
10	9.05+06	2.06-03	7.66-04	3.65-03
11	8.19+06	3.30-03	1.23-03	5.73-03
12	7.41+06	8.19-03	3.04-03	1.39-02
13	6.38+06	2.49-02	8.82-03	4.24-02
14	4.97+06	6.55-03	2.02-03	1.21-02
15	4.72+06	2.21-02	6.85-03	4.15-02
16	4.07+06	9.74-02	2.70-02	1.17-01
17	3.01+06	8.40-02	3.68-02	1.02-01
18	2.39+06	8.80-03	1.03-02	1.57-02
19	2.31+06	8.46-02	5.40-02	1.08-01
20	1.83+06	1.17-01	1.60-01	2.06-01
21	1.11+06	1.18-01	2.14-01	1.87-01
22	5.50+05	9.60-02	1.69-01	1.23-01
23	1.58+05	2.18-02	3.20-02	9.66-03
24	1.11+05	2.97-02	5.14-02	9.03-03
25	5.25+04	2.29-02	3.14-02	2.85-03
26	2.48+04	4.74-03	2.80-03	2.30-04
27	2.19+04	2.62-02	1.73-02	7.56-04
28	1.03+04	3.55-02	3.44-02	2.91-04
29	3.35+03	2.70-02	1.45-02	5.13-05
30	1.23+03	2.06-02	1.66-02	9.87-06
31	5.83+02	5.10-02	2.86-02	4.44-06
32	1.01+02	2.81-02	2.73-02	2.92-07
33	2.90+01	2.05-02	1.34-02	4.11-08
34	1.07+01	1.31-02	1.46-02	1.01-08
35	3.06+00	8.40-03	8.63-03	1.41-09
36	1.13+00	6.02-03	5.03-03	3.17-10
37	4.14-01	9.74-03	7.61-03	9.04-11
	1.00-05			

*Flux spectra presented as normalized probability distribution functions.

Table 4-18. Primary Photon Source Spectra Used in the Armed Forces Radiobiology Research Institute (AFRRI) Mixed Neutron and Photon Radiation Field Ionization Chamber Calculations

Group Number	Gamma Energy (eV)	ER1* Free Field	ER1* 15 cm Lead	^{252}Cf* Source
1	1.40+07	6.42--07	3.54–05	1.24–05
2	1.00+07	2.26--03	1.31–04	1.07–04
3	8.00+06	5.24--03	2.50–03	2.51–04
4	7.00+06	4.18--03	3.09–03	7.78–04
5	6.00+06	6.11--03	4.19–03	2.41–03
6	5.00+06	1.43--02	7.48–03	7.46–03
7	4.00+06	3.08--02	1.24–02	2.31–02
8	3.00+06	3.11--02	3.11–02	2.59–02
9	2.50+06	8.05--02	1.46–01	4.56–02
10	2.00+06	7.91--02	4.02–02	8.02–02
11	1.50+06	1.33--01	8.00–02	1.41–01
12	1.00+06	1.23--01	8.79–02	1.32–01
13	7.00+05	1.81--01	6.74–02	1.50–01
14	4.50+05	1.11--01	5.55–02	1.12–01
15	3.00+05	1.20--01	1.65–01	1.33–01
16	1.50+05	4.30--02	9.76–02	4.96–02
17	1.00+05	2.11--02	8.51–02	3.12–02
18	7.00+04	1.07--02	8.18–02	2.68–02
19	4.50+04	3.04--03	2.94–02	1.64–02
20	3.00+04	2.27--04	2.54–03	1.11–02
21	2.00+04	1.92--06	2.05–05	1.12–02
	1.00+04			

*Flux spectra presented as normalized probability distribution functions.

HEAVY and program PHOTON, respectively. Because the detector efficiency (with respect to neutron interactions) was so poor, a fictitious scattering model was incorporated in the NEUTRON program to facilitate interactions. This eliminated the capability of producing a pulse height distribution, and therefore one analog Monte Carlo case was also performed. With the fictitious scattering model, approximately 200,000 to 500,000 source particles were analyzed to obtain a fractional standard deviation less than ±10%. These cases used approximately 15 to 35 minutes of cpu time on an IBM 3033. The analog case modeled 3,000,000 source particles to obtain the same fractional standard deviation and used approximately 3 hours and 20 minutes cpu time. As in the case with the photon calibration experiments, the primary photon source spectra (Table 4-18) were modeled in program PHOTPREP to generate an input source tape for program PHOTON. The PHOTON source tape modeled 900,000 photons incident on the ionization chamber wall. The results from program HEAVY and program PHOTON were analyzed to obtain the total energy deposited in the cavity by particle type i.e., protons, alpha particles, primary photons, etc. These results were then normalized to the incident source strength to obtain the neutron, photon and total response of the ionization chamber. The cross sections and material data for the transport programs were generated using the neutron and photon cross section processor modules MICRO, MACRO, and PECSP. Recombination effects were assumed negligible, and therefore were not considered.

The comparisons of the calculated and experimental total ionization chamber responses to the mixed field experiments are

presented in Table 4-19. The calculated-to-experimental ratios (C/E) show excellent agreement in all the cases except the 0.5 cm Mg/Ar chamber in the ER1 15 cm Pb field. Like the mono-energetic photon results, the largest discrepancy (excluding the case mentioned above) occurs for the smallest measured response. A portion of this discrepancy could therefore be due to experimental error. The Monte Carlo results have a fractional standard deviation less than ±10% for all calculations. This fractional standard deviation is for the detector response per incident source particle i.e., Amps/(n-cm^2-sec-kW) or Amps/(γ-cm^2-sec-kW). To compare with the measured response, an absolute normalization was obtained from the spectra presented in Ref. 45 for the two AFRRI experiments. While the spectral shapes in Ref. 45 are probably accurate to within ±10%, the absolute normalization is known to within only ±15-20%, especially for the AFRRI ER1 15 cm Pb cases. Therefore, the MICAP calculated results in Table 4-19 are within the statistical error of the information used.

The AFRRI ER1 15 cm Pb calculation using the 0.5 cm^3 Mg/Ar ionization chamber displayed an interesting result in the neutron response analysis. In viewing the geometry description in Figure 4-17, a thin polyethylene strip (approximately 0.1-cm-high) is shown in contact with the gas region. The polyethylene acts as an insulator between the outside wall and the central electrode. The analysis of the results from program HEAVY shows recoil argon ions from neutron interactions in the gas, and proton recoils from neutron interactions with hydrogen in the polyethylene strip, as the only two sources of energy deposition in the gas. Furthermore,

Table 4-19. Comparison of Measured and Calculated Detector Responses for the Mixed Neutron and Photon Radiation Field Experiments of the Armed Forces Radiobiology Research Institute (AFRRI) Ionization Chambers

Radiation Field	Detector Volume (cm^3)	Detector Type	Calculated Response (pA)	Measured[a] Response (pA)	C/E
^{252}Cf	50	C/CO_2	6.51 (0.023)[b]	7.21	0.903
^{252}Cf	50	TE/TE	12.2 (0.062)	12.4	0.984
^{252}Cf	0.5	Mg/Ar	0.061 (0.019)	0.078	0.782
^{252}Cf	0.5	TE/TE	0.105 (0.012)	0.130	0.808
ER1 FF	0.5	Mg/Ar	7.10 (0.037)	6.42	1.11
ER1 FF	0.5	TE/TE	8.21 (0.021)	7.70	1.07
ER1 15cm Pb	0.5	Mg/Ar	4.42 (0.072)	7.16	0.617
ER1 15cm Pb	0.5	TE/TE	8.66 (0.007)	8.75	0.990

[a] Experimental uncertainty ± 5%.

[b] Fractional standard deviation $(\sigma(\bar{x})/\bar{x})$.

approximately 80% of the total signal (due to neutrons) originates from the proton recoil out of the polyethylene strip. This result is significant in that undersampling has probably occurred in the MICAP results for the polyethylene strip in the 0.5 cm^3 Mg/Ar chamber. Because the photon component of the total signal is dominant in the ^{252}Cf and in the AFRRI ER1 FF results, the undersampling would not cause a large discrepancy in a comparison of calculated and experimental total responses. The AFRRI ER1 15 cm Pb field is predominantly a neutron field however, and the 0.5 cm^3 Mg/Ar ionization chamber is designed to be highly neutron insensitive. The total response of the 0.5 cm^3 Mg/Ar ionization chamber remains dominated by the neutron component, and therefore an undersampling (and subsequent underestimation) of the neutron component would cause a significantly lower calculated value. The results appear to justify this scenario with a C/E of 0.617. A possible solution which surfaces from the above argument would be to replace the polyethylene with a non-hydrogeneous insulating material. This would mitigate the proton recoil component of the neutron signal and make the 0.5 cm^3 Mg/Ar chamber truly neutron insensitive.

The experimental results use the "two dosimeter" method described in Ref. 47 to determine the neutron and photon contribution to the total signal. Briefly, the method requires two dosimeters with different neutron sensitivities. One dosimeter, such as the TE/TE ionization chamber, will have approximately the same sensitivity to neutrons and photons. The second dosimeter, such as the Mg/Ar ionization chamber will have a reduced neutron sensitivity relative to photons. The neutron and photon components at a point

in the radiation field can be computed from the response of the two ionization chambers through the use of two simultaneous equations and the detector responses to the photon calibration experiments. MICAP on the other hand, requires only the analysis of the ionization chamber with approximately equal neutron and photon sensitivities to ascertain the relative components of the total response. A comparison of these results in Table 4-20 show excellent agreement thus reaffirming the ability of MICAP to calculate mixed field radiation experiments.

The final results presented for the mixed neutron and photon radiation fields are the pulse height distributions for the 50 cm^3 TE/TE ionization chamber in the ^{252}Cf source field. As stated earlier, only one analog Monte Carlo case was performed and therefore only one set of pulse heights are possible. The pulse height distribution due to the ^{252}Cf photon source presented in Figure 4-22 is very similar to the ^{60}Co pulse height presented in Figure 4-19. Therefore, the arguments presented with respect to the ^{60}Co pulse height distribution are equally applicable here. The pulse height distribution for the ^{252}Cf neutron source presented in Figure 4-23 depicts a continuously decreasing curve as a function of increasing energy. While there are significantly more contributions in the lower energy bins, these particles are outweighed by much larger energy depositions of the fewer particles in the higher energy bins. For the pulse height distribution shown in Figure 4-23, the average energy deposited is approximately 3.0×10^{-4} MeV/neutron. As in the case with the photon pulse height distributions, undersampling of the long high energy tail in the neutron pulse height distribution

could lead to an underestimation of the average energy deposited and therefore may lead to an inaccurate calculated value.

Table 4-20. Comparison of Measured and Calculated Detector Response Components for the Mixed Neutron and Photon Radiation Field Experiments of the Armed Forces Radiobiology Research Institute (AFRRI) Ionization Chambers

Radiation Field	Dosimeter Pair	Calculated Response Photon/Total	Measured Response[a] Photon/Total
^{252}Cf	TE/TE-C/CO_2	0.31 (0.064)[b]	0.33
^{252}Cf	TE/TE-Mg/Ar	0.26 (0.025)	0.31
ER1 FF	TE/TE-Mg/Ar	0.63 (0.012)	0.66
ER1 15cm Pb	TE/TE-Mg/Ar	0.10 (0.043)	0.09

[a] Experimental uncertainty ± 5%.

[b] Fractional standard deviation $(\sigma(\bar{x})/\bar{x})$.

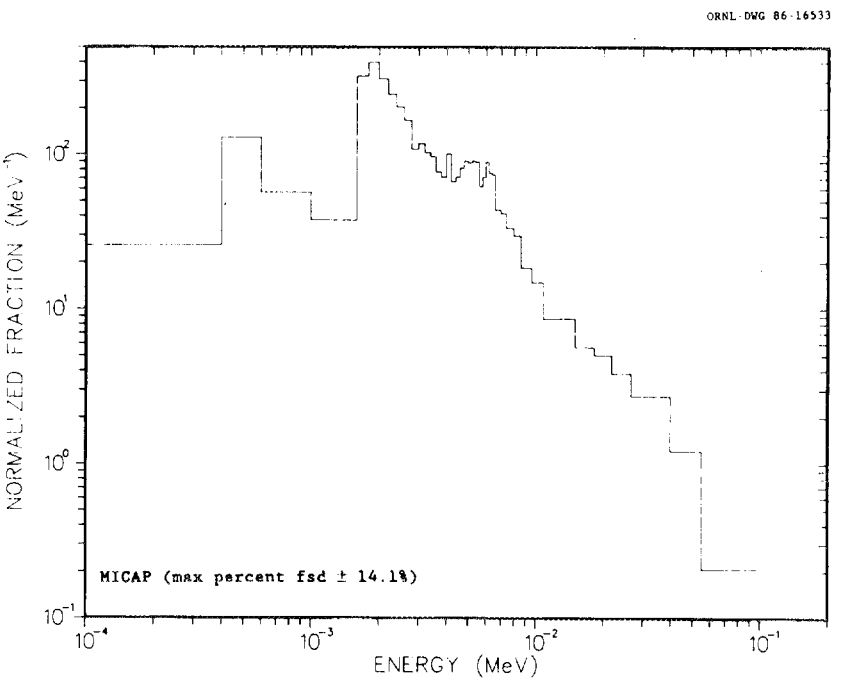

Figure 4-22. Pulse Height Distribution for the Armed Forces Radiobiology Research Institute (AFRRI) TE/TE 50 cm^3 Ionization Chamber due to a Mono-Directional ^{252}Cf Neutron Source.

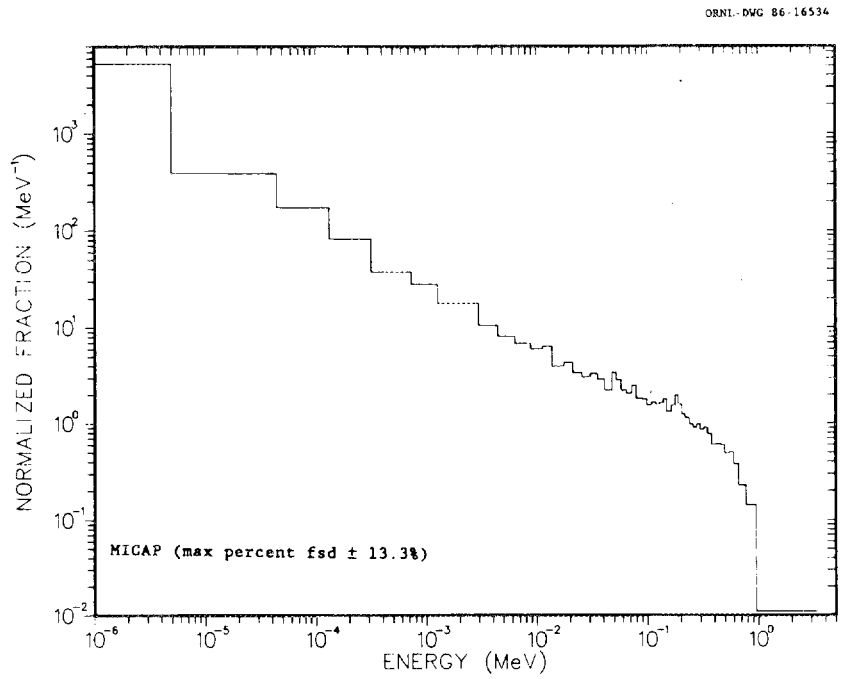

Figure 4-23. Pulse Height Distribution for the Armed Forces Radiobiology Research Institute (AFRRI) TE/TE 50 cm^3 Ionization Chamber due to a Mono-Directional ^{252}Cf Photon Source.

CHAPTER V

CONCLUSIONS

This research project has consisted of the development and verification of a new Monte Carlo code system for calculating ionization chamber responses to mixed neutron and photon radiation environments. This new code system, MICAP - Monte Carlo Ionization Chamber Analysis Package, represents a unique capability in the area of ionization chamber response analysis for mixed field dosimetry. A five part verification program was used to examine all aspects of the radiation processes applicable to ionization chamber analysis. The verification program involved comparisons with results obtained from existing codes as well as comparisons to experimental data.

The comparisons with existing codes verified the individual aspects of MICAP with respect to ionization chamber analysis. More specifically, iron transmission comparisons with MORSE yielded excellent agreement (within the Monte Carlo statistical error) in the neutron leakage spectra, secondary photon production spectra, and the photon leakage spectra for various neutron sources and iron slab thicknesses. Secondly, comparisons with MACK-IV and RECOIL data verified the nuclear models used in MICAP to describe the individual nuclear reactions with an agreement to within 10% for average energy depositions and kerma factors. Finally, the comparison to O5S, a specialized Monte Carlo detector analysis code which has been used extensively, showed excellent agreement in the pulse height distributions for a plastic scintillator, and therefore, verified the charged particle transport processes.

The comparisons with experimental data first evaluated MICAP with respect to photon calibration experiments. The results from these comparisons yielded agreement generally to within 10% for the ionization chamber responses to the mono-energetic photon sources. Finally, the comparisons with experiments performed in the mixed neutron and photon radiation environments at NBS and AFRRI verified the applicability of MICAP to mixed field ionization chamber response analysis. The calculated results agreed with experimental results to within the statistical error of the Monte Carlo and the normalization of the experimental data.

The final product (MICAP) represents a valuable tool to radiation dosimetry. The modular code system provides the most rigorous treatment to date of the particle transport processes applicable to ionization chamber response analysis. The general implementation procedures incorporated into MICAP allow the system to be useful for many applications in the field of radiation dosimetry. It is recommended that the code system be tested further by additional comparisons with mixed field radiation experiments to resolve the discrepancies noted in this document. Additional recommendations for future work are presented in the next chapter.

CHAPTER VI

RECOMMENDATIONS FOR FUTURE WORK

This study has demonstrated the applicability of using a general Monte Carlo code system for calculating an ionization chamber response to a mixed neutron and photon radiation environment. The FORTRAN code system developed and tested in this study is only a prototype, not a production code. The current version of MICAP could be improved along several lines within the present scope of ionization chamber response calculations. In particular, the following modifications and/or investigations of MICAP are suggested:

1. Improving the programming through the use of more efficient algorithms, ASSEMBLER language coding of the most cpu-intensive subroutines, and modifying program input to establish a more user friendly code system.
2. Incorporating more sophisticated and detailed charged particle evaporation models for the neutron induced charged particle production reactions i.e., (n,p), (n,α), etc. The more sophisticated models should yield a better representation of the energy of the charged particles produced via neutron interactions.
3. Performing more comparisons with mixed neutron and photon radiation experiments - especially experiments involving high energy neutron sources - to test the accuracy of the

charged particle evaporation models and further substantiate the applicability of MICAP to ionization chamber response analysis.

4. Study the incorporation of a multiple scattering capability in the low energy charged particle transport program using theoretical and empirical formulas. The current work contains only continuous energy loss models. Allowing multiple scattering in the low energy charged particle transport will yield a more accurate representation of the physics.
5. Incorporating the fictitious scattering model used in the present work as an input option to facilitate calculations involving ionization chambers which exhibit low neutron efficiency.
6. Completing the programming for the Monte Carlo source biasing to improve the calculation statistics.

Finally, MICAP could be further generalized to operate as a point Monte Carlo code system applicable to reactor core and reactor shielding calculations. This could be accomplished through program switches which engage (or dissengage) the portions of the code system applicable to a particular problem. Such a code system would truly represent a general Monte Carlo program applicable to all aspects of radiation transport/dosimetry analysis.

LIST OF REFERENCES

LIST OF REFERENCES

1. H. W. Fulbright, "Ionization Chambers," *Nuclear Instruments and Methods*, Vol 162, Nos. 1-3, Part 1, pp. 21-28, 1979.

2. T. E. Burlin, "Cavity Chamber Theory," *Radiation Dosimetry*, Vol. 1, F. H. Attix, W. C. Roesch, and E. Tochlin, Eds., Academic Press, New York, 1968.

3. *Radiation Dosimetry: X Rays and Gamma Rays with Maximum Photon Energies Between 0.6 and 50 MeV*, ICRU Report 14, International Committee on Radiation Units and Measurements, Washington, D.C., 1969.

4. *Radiation Dosimetry: X Rays Generated at Potentials of 5 to 150 keV*, ICRU Report 17, International Committee on Radiation Units and Measurements, Washington, D.C., 1970.

5. *Measurement of Absorbed Dose in a Phantom Irradiated by a Single Beam of X or Gamma Rays*, ICRU Report 23, International Committee on Radiation Units and Measurements, Washington, D.C., 1973.

6. H. Schraube, "Concluding Discussion on Ion Chambers for Neutron Dosimetry," *Ion Chambers for Neutron Dosimetry*, J. J. Broerse, Ed., EUR 6782, Commission of the European Community, Luxembourg, pp. 345-350, 1980.

7. *An International Neutron Dosimetry Intercomparison (INDI)*, ICRU Report 27, International Committee on Radiation Units and Measurements, Washington, D.C., 1978.

8. J. J. Broerse, G. Burger, and M. Coppola, *A European Neutron Dosimetry Intercomparison Project (ENDIP)*, EUR 6004, Commission of the European Community, Luxembourg, 1978.

9. H. Bichsel, J. Eenmaa, K. Weaver, and P. Wooten, "Dosimetry of Mixed Radiation Fields," proceedings of a Symposium on Biological Dosimetry, IAEA-SM-193/78, pp. 3-17, Int. Atomic Energy Agency, Vienna, 1975.

10. *Neutron Dosimetry for Biology and Medicine*, ICRU Report 26, International Committee on Radiation Units and Measurements, Washington, D.C., 1977.

11. H. Ing *et al.*, *Compendium of Neutron Spectra in Criticality Accident Dosimetry*, IAEA-180, Int. Atomic Energy Agency, Vienna, 1978.

12. J. E. Turner *et al.*, *User's Manual for PHOEL-2, A Monte Carlo Computer Code for Calculating Energies of Photoelectrons and Compton Electrons in Water*, ORNL/TM-6954, Union Carbide Corp. Nuclear Div., Oak Ridge Natl. Lab., 1979.

13. J. E. Turner *et al.*, "Calculated Electron Slowing Down Spectra for Liquid Water Irradiated by X and Gamma Rays-Implications for Photon RBE," *Sixth Symposium on Microdosimetry*, J. Booz and H. G. Ebert, Eds., Harwood Academic Publishers, London, 1978.

14. S. Pszona and M. Makarewicz, "Effect of Cavity Size on the Sensitivity of a TE-Walled, TE-Gas-Filled Ionization Chamber for Fast Neutrons," *Physics in Medicine and Biology*, Vol. 27, No. 8, pp. 1015-1022, 1982.

15. M. W. Waddell, Jr., *User's Guide to PXMORSE*, ORNL/CSD/TM-129, Union Carbide Corp. Nuclear Div., Oak Ridge Natl. Lab., 1980.

16. M. W. Waddell, Jr., "A Continuous Energy Monte Carlo Code," M.S. thesis, The University of Tennessee, Knoxville, 1980.

17. M. B. Emmett, *The MORSE Monte Carlo Radiation Transport Code System*, ORNL-4972, Union Carbide Corp. Nuclear Div., Oak Ridge Natl. Lab., 1975.

18. T. A. Gabriel, J. D. Amburgey, and B. L. Bishop, *CALOR-A Monte Carlo Program Package for the Design and Analysis of Calorimeter Systems*, ORNL/TM-5619, Union Carbide Corp. Nuclear Div., Oak Ridge Natl. Lab., 1977.

19. R. L. Ford and W. R. Nelson, *The EGS Code System: Computer Program for the Monte Carlo Simulation of Electromagnetic Cascade Showers*, SLAC-210, Stanford Linear Accelerator Center, 1978.

20. *Average Energy Required to Produce an Ion Pair*, ICRU Report 31, International Committee on Radiation Units and Measurements, Washington, D.C., 1979.

21. J. B. Birks, *The Theory and Practice of Scintillation Counting*, The Macmillian Company, New York, 1964.

22. Los Alamos Radiation Transport Group X-6, *MCNP-A Generalized Monte Carlo Code for Neutron and Photon Transport*, LA-7396-M, Los Alamos Natl. Lab., revised April 1981.

23. J. C. Nimal *et al.*, *Programme de Monte Carlo Polycinetique a Trois Dimensions*, TRIPOLI-2, C.E.A., Saclay, 1980.

24. S. N. Cramer *et al.*, *The Use of Kernels in Studying Neutron Transport Problems*, ORNL-TM-2508, Union Carbide Corp. Nuclear Div., Oak Ridge Natl. Lab., 1969.

25. D. E. Bartine *et al.*, *Low-Energy Electron Transport by the Method of Discrete Ordinates*, ORNL-TM-3438, Union Carbide Corp. Nuclear Div., Oak Ridge Natl. Lab., 1971.

26. R. Kinsey, *ENDF-102 Data Formats and Procedures for the Evaluated Nuclear Data File, ENDF/B-V*, BNL-NCS-50496, Brookhaven Natl. Lab., 1979.

27. L. L. Carter and E. D. Cashwell, *Particle Transport Simulation with the Monte Carlo Method*, TID-26607, USERDA Technical Information Center, 1975.

28. D. G. Doran and N. J. Graves, *Displacement Cross Sections and PKA Spectra: Tables and Applications*, HEDL-TME 76-70, Hanford Natl. Lab., 1976.

29. L. Dresner, *EVAP-A FORTRAN Program for Calculating the Evaporation of Various Particles from Excited Compound Nuclei*, ORNL-TM-196, Union Carbide Corp. Nuclear Div., Oak Ridge Natl. Lab., 1961.

30. P. N. Stevens and H. C. Claiborne, *Weapons Radiation Shielding Handbook*, DASA-1982-5, Defense Atomic Support Agency, Washington, D.C., 1970.

31. N. M. Schaeffer, *Reactor Shielding for Nuclear Engineers*, TID-25951, USERDA Technical Information Center, 1973.

32. T. W. Armstrong and K. C. Chandler, *SPAR A FORTRAN Program for Computing Stopping Powers and Ranges for Muons, Charged Pions, Protons, and Heavy Ions*, ORNL-4869, Union Carbide Corp. Nuclear Div., Oak Ridge Natl. Lab., 1973.

33. J. O. Johnson and T. A. Gabriel, *A User's Guide to MICAP - A Monte Carlo Ionization Chamber Analysis Package*, ORNL/TM-10340, Martin Marietta Energy Systems, Inc., Oak Ridge Natl. Lab., (to be published in 1987).

34. M. A. Abdou, Y. Gohar, and R. Q. Wright, *MACK-IV, A New Version of MACK: A Program to Calculate Nuclear Response Functions for Data in ENDF/B Format*, ANL/FPP/TM-77-5, Argonne Natl. Lab., 1978.

35. T. A. Gabriel, J. D. Amburgey, and N. M. Greene, *Radiation-Damage Calculations: Primary Recoil Spectra, Displacement Rates, and Gas-Production Rates*, ORNL/TM-5160, Union Carbide Corp. Nuclear Div., Oak Ridge Natl. Lab., 1976.

36. R. E. Textor and V. V. Verbinski, *O5S: A Monte Carlo Code for Calculating Pulse Height Distributions Due to Monoenergetic Neutrons Incident on Organic Scintillators*, ORNL-4160, Union Carbide Corp. Nuclear Div., Oak Ridge Natl. Lab., 1968.

37. S. N. Cramer and R. W. Roussin, *Monte Carlo Analysis of a Time-Dependent Neutron and Secondary Gamma Ray Integral Experiment on a Thick Concrete and Steel Shield*, ORNL/TM-7972, Union Carbide Corp. Nuclear Div., Oak Ridge Natl. Lab., 1981.

38. D. E. Bartine *et al.*, *37 Neutron, 21 Gamma Ray Coupled, P3, Multigroup Library in ANISN Format*, DLC-31/(DPL-1/FEWG1), 1975.

39. J. A. DeCampo, H. L. Beck, and P. D. Raft, *High Pressure Argon Ionization Chamber Systems for the Measurement of Environmental Radiation Exposure Rates*, HASL-260, Health and Safety Laboratory, New York, 1972.

40. 1 Lt. M. A. Dooley, Armed Forces Radiobiological Research Institute, letter to J. O. Johnson, Oak Ridge Natl. Lab., Oak Ridge, Tennessee, dated May 18 1984.

41. 1 Lt. M. A. Dooley *et al.*, "Wall Attenuation and Scatter Characteristics of Ionization Chambers at the Armed Forces Radiobiology Research Institute," draft report, Armed Forces Radiobiology Research Institute, Bethesda, Maryland, 1986.

42. D. E. Eagleson, Armed Forces Radiobiology Research Institute (AFRRI), Bethesda, Maryland, private communications to J. O. Johnson, Oak Ridge Natl. Lab., Oak Ridge, Tennessee, May-July 1986.

43. 1 Lt. M. A. Dooley *et al.*, "NBS-AFRRI Ionization Chamber Intercomparison in Mixed Neutron and Gamma-Ray Radiation Fields," TR-86-3, Armed Forces Radiobiology Research Institute, 1986.

44. J. A. Sholtis, Jr. and M. L. Moore, *Reactor Facility, Armed Forces Radiobiology Research Institute*, AFRRI TR 81-2, Armed Forces Radiobiology Research Institute, Bethesda, Maryland, 1981.

45. V. V. Verbinski and C. G. Cassapakis, *Calculation of the Neutron and Gamma-Ray Environment In and Around the AFRRI TRIGA Reactor*, DNA 5793F-2, Defense Nuclear Agency, Washington, D.C., 1981.

46. C. M. Eisenhauer, National Bureau of Standards, Washington, D. C., private communication to J. O. Johnson, Oak Ridge Natl. Lab., Oak Ridge, Tennessee, July 1986.

47. American Association of Physicists in Medicine, "Protocol for Neutron Beam Dosimetry," AAPM Report No. 7 of Task Group 18, Fast Neutron Beam Physics, Radiation Therapy Committee, 1980.

INTERNAL DISTRIBUTION

1. F. S. Alsmiller
2. R. G. Alsmiller, Jr.
3. D. E. Bartine
4. B. L. Bishop
5. T. J. Burns
6. D. G. Cacuci
7. D. H. Cook
8. S. N. Cramer
9. J. K. Dickens
10. J. D. Drischler
11. M. B. Emmett
12. W. W. Engle, Jr.
13-17. T. A. Gabriel
18. D. T. Ingersoll
19-23. J. O. Johnson
24. R. A. Lillie
25. F. C. Maienschein
26. J. V. Pace III
27. R. W. Peelle
28. F. G. Perey
29. L. M. Petrie
30. R. W. Roussin
31. J. C. Ryman
32. R. T. Santoro
33. M. S. Smith
34. J. S. Tang
35. M. W. Waddell
36. R. C. Ward
37. R. M. Westfall
38. A. Zucker
39. P. W. Dickson, Jr. (Consultant)
40. G. H. Golub (Consultant)
41. R. Haralick (Consultant)
42. D. Steiner (Consultant)
43. Central Research Library
44-48. EPMD Reports Office
49. ORNL Y-12 Technical Library Document Reference Section
50-51. Laboratory Records
52. ORNL Patent Office

EXTERNAL DISTRIBUTION

53. Dr. Charles Aeby, Air Force Weapons Laboratory, Kirkland Air Force Base, Albuquerque, NM 87117.

54. Office of Assistant Manager for Energy Research & Development, DOE-ORO, Oak Ridge, TN 37830.

55. Argonne National Laboratory, Library Services Department, 302-CE125, 9700 S. Cass Avenue, Argonne, IL 60439.

56. T. W. Armstrong, Science Applications, Inc., P.O. Box 2807, La Jolla, CA 92038.

57. Miguel Awschalom, National Accelerator Laboratory, P. O. Box 500, Batavia, IL 60510.

58. D. Berley, National Science Foundation, Washington, D.C. 20550.

59. Larry W. Brackenbush, Battelle PNL, P.O. Box 999, Richland, WA 99352.

60. Dr. J. E. Brau, Dept. of Physics, University of Tennessee, Knoxville TN 37916.

61. Brookhaven National Laboratory, Attention: Research Library, Upton, NY 11973.

62. Dr. Bruce Brown, Fermi National Accelerator Laboratory, P. O. Box 500, Batavia, IL 60510.

63. Dr. David O. Caldwell, Department of Physics, University of California at Santa Barbara, Santa Barbara, CA 93106.

64. Dr. Ernest Coleman, Office of High Energy Physics, U.S. Department of Energy, MS ER-221, Washington, D.C. 20545.

65. Stanley B. Curtis, Lawrence Radiation Laboratory, Bldg. 29, Room 213, Berkeley, CA 94720.

66. Anna Di Cicacco, Exp. VA1, CERN, CH1211, Geneva, Switzerland.

67. Herbert Destaebler, Stanford Linear Accelerator Center, Stanford University, Stanford, CA 94305.

68. Robert T. Devine, Defense Nuclear Agency, CDR, USN, Washington D.C. 20305-1000.

69. Dr. G. Dietze, Physikalisch-Technische, Bundesallee 100, D-3300 Braunschweig, WESTERN GERMANY.

70. R. D. Edge, Physics Department, University of South Carolina, Columbia, SC 29208.

71. C. M. Eisenhauer, National Bureau of Standards, Bldg. 245, Gaithersburg, MD 20899.

72. Dr. R. Eisenstein, Department of Physics, University of Illinois, Urbana, IL 61801.

73. Doug E. Engleson, Defense Nuclear Agency, Armed Forces Radiobiology Research Institute, Bethesda MD 20814.

74. Lt. Richard Engstrom, Air Force Weapons Laboratory, Kirkland Air Force Base, Albuquerque, NM 87117.

75. Dr. Chris Fabjan, CERN, Geneva 23, Switzerland.

76. Dr. G. Feldman, Stanford Linear Accelerator Center, Stanford University, Stanford, CA 94305.

77. K. Goebel, Health Physics Group, CERN, 1211 Geneva 23, Switzerland.

78. Dr. D. Hitlin, Stanford Linear Accelerator Center, Stanford University, Stanford, CA 94305.

79. Craig Jensen, Dept. of Nuclear Engineering, University of Oklahoma, Norman OK 73019.

80. Mr. Terrence Jensen, Dept. of Physics and Astronomy, The University of Rochester, Rochester, NY 14627.

81. Prof. D. Lal, Tata Institute of Fundamental Research, National Centre of the Government of India for Nuclear Science & Mathematics, Homi Bhabha Rd., Bombay 5, India.

82. Lawrence Livermore Laboratory, Technical Information Department, P.O. Box 808, Livermore, CA 94550.

83. Library for Nuclear Science, Massachusetts Institute of Technology at Middleton, Middleton, MA 01949.

84. Dr. V. S. Narasimham, Tata Institute of Fundamental Research, Bombay 400 005, India.

85. W. R. Nelson, Stanford Linear Accelerator Center, Stanford University, P. O. Box 4349, Stanford, CA 94305.

86. Keran O'Brien, Health and Safety Laboratory, U.S. Department of Energy, 376 Hudson Street, New York, NY 10014.

87. Dr. T. R. Palfrey, Jr., Department of Physics, Purdue University, West Lafayette, IN 47907.

88. Dr. Robert Palmer, Brookhaven National Laboratory, Upton, NY 11973.

89. Dr. C. W. Peck, Department of Physics, California Institute of Technology, Pasadena, CA 91109.

90. Dr. R. E. Pevey, Savannah River National Laboratory, Aiken SC 29808.

91. Dr. David W. O. Rogers, Head, Ionizing Radiation Standards, Division of Physics, National Research Council of Canada, Ottawa, Canada K1A0R6.

92. Dr. C. Rubbia, Lyman Laboratory, Harvard University, Cambridge, MA 02138.

93. Dr. W. Schmidt, Institute of Experimental Nuclear Physics, University of Karlsruhe, 75 Karlsruhe, W. Germany.

94. The Secretary, Radiation Group, Lab II, CERN, 1211 Geneva 23, Switzerland.

95. Dr. Walter Selove, University of Pennsylvania, Department of Physics, Philadelphia, PA 19104.

96. B. S. P. Shen, Department of Astronomy, University of Pennsylvania, Philadelphia, PA 19104.

97. Stanford Linear Accelerator Center, Attention: Library, P. O. Box 4349, Stanford, CA 94305.

98. Dr. Alan Stevens, Accelerator Dept. Bldg. 911, Brookhaven National Laboratory, Upton, NY 11973.

99. G. R. Stevenson, Radiation Protection Group, Lab II, CERN, 1211 Geneva 23, Switzerland.

100. Dr. L. Sulak, Department of Physics, University of Michigan, Ann Arbor, MI 48109.

101. R. Tesch, DESY, Hamburg, Notkesteig 1, W. Germany.

102. Ralph H. Thomas, Lawrence Berkeley Laboratory, Occupational Health Office, 50A-5106, Engineering Division, Berkeley, CA 94720.

103. Dr. W. J. Willis, CERN, Geneva 23, Switzerland.

104. Dr. S. Yellin, Stanford University, Stanford Linear Accelerator Center, P. O. Box 4349, Stanford, CA 94305.

105. G. B. Yodh, University of Maryland, College Park, MD 20742.

106. Robert Young, Director, Defense Nuclear Agency, ATTN: STRP, 6801 Telegraph Road, Alexandria, VA 22310.

107. Dr. B. Zeitnitz, Nuclear Research Center, Karlsruhe, W. Germany 93120.

108. Gary H. Zeman, Defense Nuclear Agency, CDR, MSC, USN, Armed Forces Radiobiology Research Institute, Bethesda MD 20814.

109-343. Defense Nuclear Agency Transport Distribution (AU).

344-373. Technical Information Center, Oak Ridge Turnpike, Oak Ridge TN 37830.